

Role of flow topology in wind-driven wildfire propagation

Siva Viknesh^{1,2} Ali Tohidi^{3,4} Fatemeh Afghah⁵ Rob Stoll¹
Amirhossein Arzani^{1,2}

¹ Department of Mechanical Engineering, University of Utah, Salt Lake City, UT, USA

² Scientific Computing & Imaging Institute, University of Utah, Salt Lake City, UT, USA

³ Department of Mechanical Engineering, San José State University, San José, CA, USA

⁴ Wildfire Interdisciplinary Research Center (WIRC), San José State University, San José, CA, USA

⁵ Department of Electrical and Computer Engineering, Clemson University, Clemson, SC, USA

Correspondence:

Amirhossein Arzani,

University of Utah,

Salt Lake City, UT, 84112

Email: amir.arzani@sci.utah.edu

Abstract

Wildfires propagate through intricate interactions between wind, fuel, and terrain, resulting in complex behaviors that pose challenges for accurate predictions. This study investigates the interaction between wind velocity topology and wildfire spread dynamics, aiming to enhance our understanding of wildfire spread patterns. We revisited the non-dimensionalization of the governing combustion model by incorporating three distinct time scales. This approach revealed two new non-dimensional numbers, contrasting with the conventional non-dimensionalization that considers only a single time scale. Through scaling analysis, we analytically identified the critical determinants of transient wildfire behavior and established a state-neutral curve, indicating where initial wildfires extinguish for specific combinations of the identified non-dimensional numbers. Subsequently, a wildfire transport solver was developed using a finite difference method, integrating compact schemes and implicit-explicit Runge-Kutta methods. We explored the influence of stable and unstable manifolds in wind velocity on the transport of wildfire under steady wind conditions defined using a saddle-type fixed point flow, emphasizing the role of the non-dimensional numbers. Additionally, we considered the benchmark unsteady double-gyre flow and examined the effect of unsteady wind topology on wildfire propagation, and quantified the wildfire response to varying wind oscillation frequencies and amplitudes using a transfer function approach. The results were also compared to Lagrangian coherent structures (LCS) used to characterize the correspondence of manifolds with wildfire propagation. The comprehensive approach of utilizing the manifolds computed from wind topology provides valuable insights into wildfire dynamics across diverse wind scenarios, offering a potential tool for improved predictive modeling and management strategies.

Keywords: Wildland fire, Wind topology, Combustion, Firefront, Lagrangian coherent structures, reactive flows

1 Introduction

Wildfires have long been integral to earth’s ecological processes, playing a crucial role in shaping habitat dynamics and ecosystem structures since the emergence of terrestrial vegetation. While many ecosystems rely on periodic wildfires to maintain their ecological balance, these events also pose significant threats to human infrastructure and safety, with uncontrolled and extensive wildfires often leading to catastrophic property damage, loss of life, and severe degradation of air quality.

Wildfires represent a unique form of thermal-degradation of fuels followed by natural combustion, characterized by a self-regulating fuel supply rate intrinsically linked to the fire’s behavior. Unlike other combustion processes, wildland fires rely on positive feedback mechanisms, where the intense heat generated during combustion significantly influences fire spread, with convection and thermal radiation often playing a pivotal role (Finney et al., 2015). The propagation of wildfires is generally classified into two categories: plume-driven and wind-driven fires (Byram, 1959; Morvan and Frangieh, 2018). Wind-driven fires are particularly hazardous due to their rapid propagation and high potential for ember casting (also known as firebrand showers), which complicates the evolution of fire spread even further due to the highly transient and intrinsically stochastic behavior (Tarifa et al., 1965; Koo et al., 2010; Tohidi and Kaye, 2017). The dynamics of wildfires encompass two critical stages: ignition and the propagation of the fire front across different fuel types, particularly live fuels. Neither of these processes is fully understood or extensively explored, as various physical parameters, including the structure and condition of vegetation, topography, and atmospheric conditions such as wind patterns, air temperature, and relative humidity strongly influence them (Boroujeni et al., 2024; Powers et al., 2017).

Mathematical models of wildfires provide crucial insights into the complex interactions between the firefront, vegetation, and wind patterns, which collectively constitute the fundamental mechanisms driving wildfire ignition and progression. In a comprehensive review, Sullivan (2009a) detailed the development of physics-based wildfire models, while Sullivan (2009b) explored empirical and quasi-empirical models, with challenges and limitations in accurately simulating fire behavior discussed in Sullivan (2009c) and Or et al. (2023). In the present work, we focus on continuum physics-based wildfire models and specifically the nonlinear convection-diffusion-reaction (CDR) model proposed in Asensio and Ferragut (2002). The mathematical properties of the nonlinear CDR wildfire model, including the existence of traveling wave solutions and uniqueness of solutions, are established in Asensio and Ferragut (2002). Notably, Babak et al. (2009) investigated the profound impact of wind direction on the firefront’s advection within a one-dimensional analytical framework, demonstrating that wind could either accelerate or decelerate fire progression depending on its flow direction while affirming the uniqueness of solutions under varying wind conditions. Similarly, Reisch et al. (2024) investigated the influence of diffusion and reaction parameters, along with wind speed, on wildfire propagation speed, unburned biomass fuel, and maximum achievable fire temperature by examining various simplified sub-models within the wildfire CDR framework.

Numerous studies have explored the influence of wind direction on wildfire behavior. Fendell and Wolff (2001) introduced an empirical mathematical expression that relates unidirectional wind speed to the fire spread rate for a given fuel load, based on quasi-steady firefront propagation experiments. In related work, Rossa and Fernandes (2018) developed an empirical model that accounts for wind effects, examining various fuels and their spatial orientations relative to the wind. Atchley et al. (2021) further advanced these studies by investigating the spatially heterogeneous distribution of fuel, while Simpson et al. (2013); Li et al. (2021) analyzed the influence of terrain slope on wildfire dynamics. Notably, Sun et al. (2009) investigated fire-boundary layer interactions through a fully coupled wildfire-atmosphere large eddy simulation for grassland fires. Their study highlighted how

a roll-dominated atmospheric boundary layer and its intricate local flow features could influence fire spread and how the fire, in turn, affects the boundary layer. Filippi et al. (2018) further corroborated the interaction between the fire and boundary layer by performing multi-scale high-resolution large-eddy wildfire simulations, revealing the significance of intricate turbulence effects. Similarly, Bürger et al. (2020) demonstrated that even minor quasi-temporal variations in wind direction can significantly alter both the propagation direction and the spread length of wildfires.

Despite the growing interest in wind-driven wildfire transport, our understanding of how coherent flow structures in wind influence wildfire propagation patterns remains limited. This paper aims to address this gap by leveraging concepts from dynamical systems theory to identify and predict “coherent patterns” in wind-driven wildfire propagation. In particular, stable and unstable manifolds, identified using Lagrangian coherent structures (LCS), have been utilized in the past to identify templates for convective transport (Shadden et al., 2005; Allshouse and Peacock, 2015; Haller, 2015). LCS has been applied across various fields, including biomedical (Arzani and Shadden, 2012), turbulent (Wilson et al., 2013), environmental (BozorgMagham et al., 2013), and reactive flows (Mahoney et al., 2012). Within the context of wildfires, recent studies from the atmospheric science community have employed the LCS framework to qualitatively predict the evolution of smoke plumes from wildfire events (Curbelo and Rypina, 2023; Allen et al., 2024; Jarvis et al., 2024). However, the direct relevance of LCS to wildfire propagation has yet to be explored. Given that wildfire transport is not purely advective, it remains unclear how flow topology can be utilized and under what conditions its role becomes significant. Gaining such fundamental insights is crucial, as it enables the prediction of wildfire growth patterns without the need to solve computationally expensive transport problems, assuming the wind velocity field is known. The attracting LCS (unstable manifolds) tend to draw transported material, such as fire lines, towards themselves, which could indicate regions of heightened risk. Conversely, the repelling LCS (stable manifolds) may potentially push fire lines away, thereby creating safer zones for positioning firefighters.

In this paper, we consider the Asenio wildfire model (Asensio and Ferragut, 2002), which incorporates key pathways in wildfire transport, including wind-driven convection, nonlinear diffusion due to heat and radiation, fuel-limited reaction, and simplified natural convection. The model, however, does not account for several critical factors, such as terrain slope (Coen, 2018) and firebrands (Tohidi and Kaye, 2017). Additionally, we assume the wind velocity is known and provided, thereby neglecting the heating-induced buoyancy forces that can alter wind velocity—factors that have been incorporated in more complex coupled weather–wildland models (Mandel et al., 2011; Coen et al., 2013; Coen, 2015). While we acknowledge the relative simplicity of the Asenio model, especially given the multiscale nature of wildfires (Hädlich et al., 2021; Hudson et al., 2020), this simplicity allows us to focus on the fundamental factors and understand the role of flow topology in the interplay between key physical processes (reported using nondimensional groups). From a fundamental perspective, we approach the problem by modeling nonlinear convection-diffusion-reaction transport, where limited fuel (vegetation) acts as a source (reaction term) sustaining the high-temperature fire spread. This approach prioritizes a fundamental reactive flow mindset over a realistic, wildfire-specific modeling approach. The precise flame and combustion chemistry are not modeled, as these phenomena occur on scales much smaller than those at which wind velocity data is typically measured or modeled. Nonetheless, understanding the behavior of this particular class of reacting flows will lay the groundwork for developing more complex models in the future.

The paper is organized as follows: In Section 2, we revisit the wildfire spread model presented by Asensio and Ferragut (2002) and proceed to non-dimensionalize it, introducing previously unrecognized dimensionless numbers. This section also details the development of a wildfire transport solver based on finite difference methods. Section 3 presents a scaling analysis to identify the key

factors influencing wildfire behavior. In Section 4, we explore the characteristics of transient wildfire dynamics under steady wind conditions with saddle-type fixed points and analyze the impact of unsteady wind velocities modeled by a double-gyre flow.

2 Methods

2.1 Mathematical wildfire model

The mathematical nonlinear convection-diffusion-reaction model for wildland fire propagation, proposed by Asensio and Ferragut (2002), is based on the principles of energy and species conservation, considering the quantity of fuel while disregarding its specific intricate composition. The reaction rate (r) in this model is characterized by the Arrhenius equation, $r = A \exp(-E_A/(RT))$, and the fuel burning rate (S_Y) is proportional to this reaction. In wildfire scenarios, sub-grid radiation flux through fuel parcels is an important mode of heat transfer, characterized by the Stefan-Boltzmann law, $q_{\text{rad}} = 4\sigma\delta T^3$. Furthermore, natural convection is encapsulated by Newton's law of cooling, $q_{\text{conv}} = h(T - T_\infty)$. Integrating these components—convection, radiation, reaction, and natural convection—the proposed one-way coupled model for flame propagation and fuel burning is mathematically formulated as

$$\rho C \frac{\partial T}{\partial t} + \underbrace{\rho C (\vec{\nabla} \cdot \nabla T)}_{\text{Convection}} = \underbrace{\nabla \cdot ((4\sigma\delta T^3 + k)\nabla T)}_{\text{Diffusion}} + \underbrace{s(T)^+ \rho Y H r}_{\text{Reaction}} - \underbrace{h(T - T_\infty)}_{\text{Natural Convection}} \quad (1a)$$

$$\frac{\partial Y}{\partial t} = -s(T)^+ Y A e^{-E_A/RT}, \quad (1b)$$

where ρ is the density of air, C is the constant pressure specific heat, T is the absolute temperature, $\vec{\nabla}$ is the velocity vector, σ stands for the Stefan-Boltzmann constant, δ represents the optical path length for radiation, k indicates thermal conductivity, $s(T)^+$ characterizes the dimensional phase change function, Y is the fuel mass fraction, H represents the heat of combustion, r is the reaction rate, h is the natural heat convection coefficient, T_∞ stands for the ambient temperature, A represents the pre-exponential factor for a first order kinetic scheme, E_A is the activation energy, and R is the universal gas constant.

The mathematical model was originally non-dimensionalized using the Frank-Kamenetskii change of variables method, considering only one characteristic temporal scale (t_0) and spatial scale (l_0). It involves applying the following change of variables to non-dimensionalize the wildfire equation.

$$\xi = \frac{x}{l_0}, \quad \eta = \frac{y}{l_0}, \quad \tau = \frac{t}{t_0}, \quad \bar{T} = \frac{T - T_\infty}{\epsilon T_\infty}, \quad \beta = \frac{Y}{Y(t_0)}, \quad \vec{\mathbf{w}} = \frac{t_0}{l_0} \vec{\nabla}, \quad (2)$$

where ξ and η represent the normalized spatial lengths along the x and y directions, respectively, using the characteristic length scale $l_0 = \sqrt{(t_0 k)/(\rho C)}$. τ denotes the dimensionless evolution time normalized using the characteristic temporal scale $t_0 = (e^{(1/\epsilon)} \epsilon)/(qA)$, where $\epsilon = (RT_\infty)/(E_A)$ represents the inverse activation energy and $q = (HY_0)/(CT_\infty)$ is the non-dimensional reaction heat. In addition, $\vec{\mathbf{w}}$ denotes the normalized velocity, and β represents the normalized fuel mass fraction. Using the non-dimensional absolute temperature (\bar{T}) and non-dimensional phase temperature (\bar{T}_{pc}), the non-dimensional phase function is defined as

$$s(\bar{T})^+ = \begin{cases} 1 & \text{if } \bar{T} \geq \bar{T}_{\text{pc}} \\ 0 & \text{otherwise} \end{cases} \quad \text{with} \quad \bar{T}_{\text{pc}} = \frac{T_{\text{pc}} - T_{\infty}}{\epsilon T_{\infty}}. \quad (3)$$

By using the above change of variables, the non-dimensional form of the wildfire transport model for temperature and fuel consumption fields is obtained as follows

$$\frac{\partial \bar{T}}{\partial \tau} + \vec{\mathbf{w}} \cdot \nabla \bar{T} = \nabla \cdot (K(\bar{T}) \nabla \bar{T}) + f(\bar{T}, \beta), \quad (4a)$$

$$\frac{\partial \beta}{\partial \tau} = -s(\bar{T})^+ + \frac{\epsilon}{q} \beta e^{\bar{T}/(1+\epsilon \bar{T})}, \quad (4b)$$

where $K(\bar{T}) = \bar{\kappa}(1 + \epsilon \bar{T})^3 + 1$ and $f(\bar{T}, \beta) = s(\bar{T})^+ \beta e^{\bar{T}/(1+\epsilon \bar{T})} - \alpha \bar{T}$ are defined using the non-dimensional natural convection coefficient $\alpha = (t_0 h)/(\rho C)$ and the inverse non-dimensional conductivity coefficient $\bar{\kappa} = (4\sigma \delta T_{\infty}^3)/k$. We may enforce the following zero-flux Robin boundary condition at the domain boundaries, given that the boundary is assumed to prevent wildfire propagation beyond the boundary

$$(\vec{\mathbf{w}} \bar{T} - K(\bar{T}) \nabla \bar{T}) \cdot \hat{\mathbf{n}} = 0. \quad (5)$$

Finally, the stability of the numerical methods used to solve the wildfire equation can be assessed by observing the highest temperature (\bar{T}_{max}) over time. For highly accurate numerical schemes, this peak temperature should closely match, but not exceed, the maximum temperature predicted by the zero-dimensional non-diffusive combustion model at the initialized time instant, as expressed by

$$\bar{T}_{\text{max}} = \frac{q}{\epsilon} \left(\beta + \frac{\epsilon}{q} \bar{T} \right). \quad (6)$$

2.2 New non-dimensional wildfire model

In the wildfire model described by Eq. 1, three distinct characteristic temporal scales are evident: fuel reaction (t_r), flow convection (t_f), and diffusion (t_d). However, Asensio and Ferragut (2002) assumed these temporal scales to be identical when using the Frank-Kamenetskii method to derive the non-dimensionalized form of the wildfire equation shown in Eq. 4. Here, we define the three distinct characteristic temporal scales for the different processes according to Frank-Kamenetskii theory, along with the wind velocity:

$$t_d = \frac{\rho C l_0^2}{k}, \quad t_r = t_0 = \frac{\epsilon e^{(1/\epsilon)}}{q A}, \quad t_f = \frac{l_0}{U_{\infty}}, \quad \vec{\mathbf{w}} = \frac{\vec{\mathbf{V}}}{U_{\infty}}. \quad (7)$$

By incorporating the three temporal scales, the velocity scale normalized using U_{∞} representing the freestream velocity, and the change of variables outlined in Eq. 2, we derive the new non-dimensional form of the wildfire equation as follows

$$\frac{\partial \bar{T}}{\partial \tau} + \frac{\vec{\mathbf{w}}}{\Phi} \cdot \nabla \bar{T} = \frac{1}{Da} \nabla \cdot (K(\bar{T}) \nabla \bar{T}) + f(\bar{T}, \beta), \quad (8a)$$

$$\frac{\partial \beta}{\partial \tau} = -s(\bar{T})^+ + \frac{\epsilon}{q} \beta e^{\bar{T}/(1+\epsilon \bar{T})}. \quad (8b)$$

In this context, the Damköhler number $Da = t_d/t_r = (\rho Cl_0^2 q A)/(\epsilon e^{(1/\epsilon)} k)$ represents the ratio of the diffusion time scale to the reaction time scale, indicating how fast the reaction rate is in comparison to the diffusion rate. Similarly, Peclet number $Pe = t_d/t_f = (\rho C U_\infty l_0)/k$ signifies the ratio of the diffusion time scale to the flow convection time scale, elucidating the relationship between convection and diffusion. Furthermore, a new non-dimensional number, $\Phi = t_f/t_r = Da/Pe$, has been identified and defined as the ratio of flow convection rate to reaction rate, thus establishing a relationship between the Damköhler number and the Peclet number. This process of non-dimensionalization has unveiled a previously unnoticed new non-dimensional number (Φ) and Damköhler number inherent within the wildfire combustion model under consideration. It is imperative to underscore that the resulting new non-dimensional combustion model (Eq. 8) reduces to the conventional form represented by Eq. 4 in instances where both Da and Φ values converge to 1. Based on reported data in the literature (Asensio and Ferragut, 2002; Fendell and Wolff, 2001; Bürger et al., 2020; Amini et al., 2019; Cheney et al., 2012), practical wildfire scenarios typically exhibit Da ranging from 1 to 10^3 , influenced by a pre-exponential factor (A) between 10^9 and 10^{12} and an inverse activation energy $\epsilon \approx 0.03$. Similarly, Φ varies from 10^{-1} to 10^{-6} , which corresponds to wind speeds from 0.01 m/s to 25 m/s, spanning from very calm to extreme conditions. In this study, the newly derived non-dimensional wildfire equation is employed to investigate fire propagation under various wind conditions, with Da ranging from 1 to 10^3 and ϵ between 0.03 and 0.045. Our focus is on wind topologies associated with moderate wind speeds (Cheney et al., 2012), where Φ ranges from 10^{-1} to 10^{-3} , corresponding to wind speeds from 0.1 m/s to 10 m/s, with A set to 10^{12} (less diffusion) to represent this moderate wind speed regime. It is anticipated that in scenarios with significantly stronger winds, the influence of convection and wind topology on wildfire propagation will become increasingly pronounced.

2.3 Numerical methods

In this section, we present our approach to solving the wildfire model using the finite difference method (FDM), with the additional advantage of leveraging CUDA support to facilitate simulations on GPUs. We implement an upwind compact scheme for the advective term to maintain its upwinding properties and employ central difference schemes for the diffusion term to accurately mirror its isotropic nature. Given the inherent numerical stiffness of the wildfire equation, we utilize the Implicit-Explicit Runge-Kutta (IMEX-RK) method for temporal integration, carefully distinguishing between stiff and non-stiff terms within the newly non-dimensionalized wildfire equation. Additionally, we incorporate a localized artificial diffusivity model to mitigate numerical instabilities, which is discussed below. The validation of our developed FDM solver is presented in Appendix B.

2.3.1 Upwind compact FDM scheme

The compact schemes with spectral-like resolution were initially introduced by Lele (1992) within the FDM framework. While this scheme exhibits superior performance for periodic boundary conditions due to its implicit nature, it tends to manifest numerical instabilities such as anti-diffusion and anti-dissipation near the domain boundaries when applied to non-periodic problems. Furthermore, optimization of the compact scheme for fluid flow problems was conducted by Sengupta et al. (2003) through global spectral analysis, where the near-boundary numerical instabilities for non-periodic problems were mitigated by the development of higher-order explicit upwind boundary closures, effectively resolving length scales without the need for numerical filtering or damping. The

optimized upwind compact scheme (OUCS2) utilized for computing the first derivative advection term at interior grid points is expressed as follows

$$p_{i-1}T'_{i-1} + T'_i + p_{i+1}T'_{i+1} = \frac{1}{h_x} \sum_{m=-2}^2 s_m T_{i+m}, \quad (9)$$

where T'_i represents the spatial derivative calculated using the information of T_i at a given i^{th} node for the grid spacing of h_x . The other relevant coefficient values are given by

$$\begin{aligned} p_{i\pm 1} &= D \pm \frac{\hat{\eta}}{60}, & s_{\pm 2} &= \pm \frac{F}{4} + \frac{\hat{\eta}}{300}, & s_{\pm 1} &= \pm \frac{E}{2} + \frac{\hat{\eta}}{30}, & s_0 &= -\frac{11\hat{\eta}}{150}, \\ D &= 0.3793894912, & F &= 1.57557379, & E &= 0.183205192, & \hat{\eta} &= -2. \end{aligned}$$

2.3.2 IMEX-RK method

The fuel reaction term in the wildfire equation imposes a more severe time-step restriction than the diffusion term, which makes the long-time simulation laborious when one uses a fully explicit time integration method, and it becomes intractable for a fully implicit time integration scheme where one has to solve a system of nonlinear equations. On the other hand, the splitting technique may be helpful for solving the wildfire transport equation with the dynamics at different time scales, provided spatio-temporal balancing is ensured over time. The IMEX-RK schemes provide a viable strategy to integrate stiff and non-stiff terms of an equation, *simultaneously*, using an implicit and explicit temporal scheme, respectively. In this work, we employed the robust L-stable IMEX-RK3 scheme outlined by Pareschi and Russo (2005) for temporal integration across all wildfire simulations investigated. Notably, Bürger et al. (2020) introduced the IMEX-RK temporal scheme for the wildfire equation while identifying stiff and non-stiff terms for the first time, and we extended their algorithm to accommodate the new non-dimensional form of the equation, presented in Appendix A. We highlight the stiff (\bar{T}) and non-stiff non-dimensional temperature (\hat{T}) components within our newly derived non-dimensional wildfire equation, given as follows:

$$\frac{\partial \bar{T}}{\partial \tau} = \frac{1}{Da} \nabla \cdot (K(\hat{T}) \nabla \bar{T}) + s(\hat{T}) + \beta e^{\hat{T}/(1+\epsilon\hat{T})} - \alpha \bar{T} - \frac{\vec{\mathbf{w}}}{\Phi} \cdot \nabla \hat{T}, \quad (10a)$$

$$\frac{\partial \beta}{\partial \tau} = -s(\hat{T}) + \frac{\epsilon}{q} \beta e^{\hat{T}/(1+\epsilon\hat{T})}. \quad (10b)$$

2.3.3 Localized artificial diffusivity model

In wildfire transport, the propagation of a firefront often manifests as a discontinuous wave, leading to the excitation of high-frequency numerical instabilities due to Gibbs' phenomenon in the vicinity of the firefront across the given fuel field. This poses a challenge for obtaining a tractable numerical solution, necessitating the use of artificial diffusion to enable very long-time integration, particularly in situations with very *low* Φ values—indicative of high wind velocities. In resolving the advecting firefront, it is crucial to maintain high accuracy in regions where the solution is smooth while ensuring stability at discontinuities. To address this, we employ a localized artificial diffusion approach to attenuate high-frequency modes near the resolution limit without compromising lower-frequency ones. This method introduces artificial diffusion that varies spatially, targeting sharp

discontinuities identified through higher-order spatial derivative values. Leveraging the localized artificial diffusion (LAD) model proposed by Aslani and Regele (2018), we delineate the firefront and smooth regions employing the Heaviside function (\mathbf{H}_F) applied to the absolute fourth derivative of the temperature field, resulting in a calculation of localized artificial diffusion coefficient (μ). Given that temperature is a scalar field, we observed that further application of Gaussian filtration is unnecessary and does not impact accuracy, thus saving computational time. The localized artificial diffusivity model used in the present work is given as follows

$$\Delta_T^2 = \mu \nabla^2 \bar{T} \quad , \quad \mu = C_\mu \mathbf{H}_F(|\nabla^4 \bar{T}|) . \quad (11)$$

2.4 Lagrangian coherent structures

Lagrangian coherent structures (LCS) are pivotal in the study of complex dynamical systems (Haller and Yuan, 2000), particularly in fluid dynamics, where they serve as organizing templates for unsteady flows and govern the transport and mixing of passive particles over time. The simplest numerical approach for detecting LCS is through the finite-time Lyapunov exponent (FTLE) fields (Shadden, 2011), which quantify the rate of separation of infinitesimally close trajectories over a finite time interval. The ridges of the FTLE field (locally maximum FTLE in the transverse direction) delineate the LCS and partition regions within the flow field that exhibit distinct flow behavior.

Given a velocity field $\mathbf{u}(\mathbf{x}, t)$ describing the flow, the trajectory $\mathbf{x}(t)$ of a particle starting at position \mathbf{x}_0 at time \hat{t}_0 is governed by the ordinary differential equation

$$\frac{d\mathbf{x}}{dt} = \mathbf{u}(\mathbf{x}, t) . \quad (12)$$

To quantify the separation between nearby trajectories, the Cauchy-Green strain tensor $\widehat{\mathbf{C}}_{\hat{t}_0}^{t_1}(\mathbf{x}_0)$ is computed as:

$$\widehat{\mathbf{C}}_{\hat{t}_0}^{t_1}(\mathbf{x}_0) = \left(\frac{\partial \mathbf{x}(t)}{\partial \mathbf{x}_0} \right)^\top \frac{\partial \mathbf{x}(t)}{\partial \mathbf{x}_0} , \quad (13)$$

where $\frac{\partial \mathbf{x}(t)}{\partial \mathbf{x}_0}$ represents the flow map gradient, describing how initial positions evolve over time. The largest eigenvalue $\bar{\lambda}_{\max}$ of the Cauchy-Green tensor defines the FTLE as

$$\widehat{\sigma}_{\hat{t}_0}^{t_1}(\mathbf{x}_0) = \frac{1}{|t_1 - \hat{t}_0|} \ln \sqrt{\bar{\lambda}_{\max}} . \quad (14)$$

The ridges of the FTLE field, $\widehat{\sigma}_{\hat{t}_0}^{t_1}(\mathbf{x}_0)$, signify the presence of LCS, delineating boundaries between regions exhibiting distinct Lagrangian behavior. In the present work, where we consider the 2D unsteady double-gyre, the FTLE fields were computed using the TBarrier package (Bartos et al., 2023). It is important to acknowledge that the LCS is based on passive transport by the velocity field, which does not fully apply to wildfires. Our objective here is to explore the extent to which LCS can influence firefront propagation. Future research should focus on developing generalized LCS frameworks (Balasuriya et al., 2018) to improve the correspondence with wildfires.

3 Scaling analysis

First, we perform a scaling analysis to understand the influence of the dimensionless parameters on combustion dynamics within the newly derived non-dimensional wildfire equation. Below, we

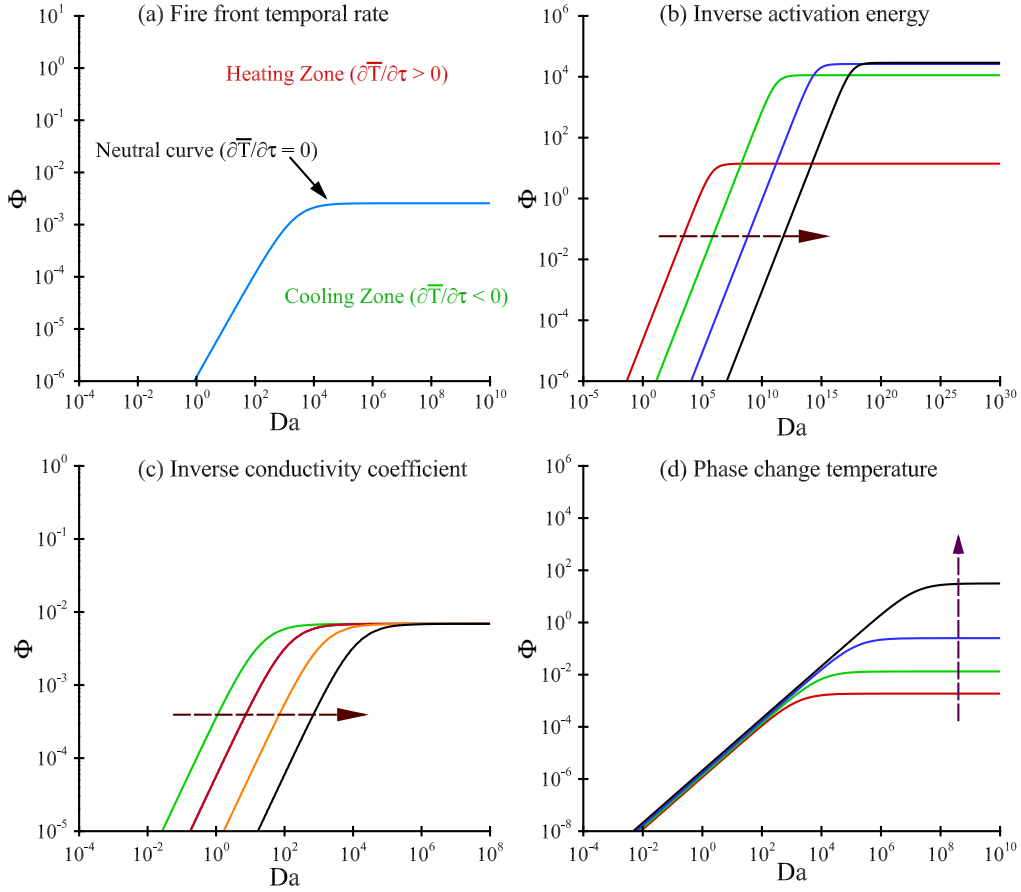


Figure 1: Temporal evolution of the initialized firefront temperature under the influence of various parameters. (a) A zero-valued contour of $\partial\bar{T}/\partial\tau$ is highlighted, representing the neutral curve along with the heating ($\partial\bar{T}/\partial\tau > 0$) and cooling ($\partial\bar{T}/\partial\tau < 0$) zones over the Da - Φ non-dimensional plane. (b) Inverse activation energy ϵ , (c) inverse non-dimensional conductivity coefficient $\bar{\kappa}$, and (d) non-dimensional phase change temperature \bar{T}_{pc} are shown in the same plane. The dotted arrows indicate the incremented directions of these dimensionless parameters.

introduce characteristic scales that, under the specified assumptions, transform the spatial derivative terms in the differential equations into an algebraic form. This analytical process provides valuable insights into the relative significance of various terms and parameters, thereby unveiling the critical determinants governing transient wildfire behavior. The chosen characteristic scales for scaling analysis are as follows

$$\bar{T} \sim \bar{T}_{\max}, \quad \nabla\bar{T} \sim \frac{(\bar{T}_{\max} - \bar{T}_{pc})}{\bar{h}_x} = \bar{T}_{\Delta}, \quad \beta \sim \beta_{\max}, \quad |\vec{w}| \sim U_{\infty}. \quad (15)$$

Utilizing the established characteristic scales for temperature and fuel, we proceed with the following assumptions for the scaling analysis: (i) Uniform wind velocity is assumed using the U_{∞} scale, disregarding spatial velocity gradients. (ii) The firefront consistently attains \bar{T}_{\max} regardless of fuel spatial distribution. (iii) A maximum value of fuel distribution (β_{\max}) is assumed everywhere, ignoring heterogeneous distribution across space. (iv) Assuming that the firefront thickness (\bar{h}_x) is temporally invariant, the temperature gradient is approximated as the difference between \bar{T}_{\max} and \bar{T}_{pc} over the firefront thickness. Moreover, \bar{T}_{\max} can be calculated using the analytical formulation given in Eq. 6. Under these conditions, we derive the algebraic form of Eq. 8, representing the

temporal evolution of initialized firefront temperature, as given below

$$\frac{\partial \bar{T}}{\partial \tau} \sim \underbrace{\frac{1}{Da} \left\{ \bar{T}_\Delta^2 [3\bar{\kappa}\epsilon(1 + \epsilon\bar{T}_{\max})^2] + K \frac{\bar{T}_\Delta}{h_x} \right\}}_{\text{Heating term}} + \beta_{\max} e^{\bar{T}_{\max}} - \underbrace{\left[\frac{U_\infty}{\Phi} \bar{T}_\Delta + \alpha \bar{T}_{\max} \right]}_{\text{Cooling term}}. \quad (16)$$

Based on the temperature temporal rate expressed in Eq. 16, it is observed that diffusion and reaction processes provide the energy required to heat the initialized firefront, while natural and forced convection processes remove heat energy, cooling the firefront. Interestingly, for certain combinations of the Da and Φ numbers, along with other given dimensionless parameters, these heating and cooling processes balance each other. At this balance point, the fire neither grows nor decays from its initialized strength, a state referred to as the neutral curve, as shown in Fig. 1(a). In other words, the neutral curve represents a state where the temperature's temporal rate, $\partial \bar{T} / \partial \tau$, is zero, demarcating the zones on the Da - Φ plane where heating ($\partial \bar{T} / \partial \tau > 0$) and cooling ($\partial \bar{T} / \partial \tau < 0$) occur. Notably, when depicted on a log-log scale, the neutral curve exhibits a nearly linear growth, particularly saturating at higher Da values. Furthermore, a power law fitting analysis was conducted, expressing $\Phi = mDa^n$, to quantitatively characterize this growth behavior. This mathematical regression yielded an exponent value of $n = 0.8564$ (slope in log-log scale) and an amplitude of $m = 5.882 \times 10^{-5}$ (offset in log-log scale), providing valuable insights into the intricate relationship between Da and Φ regarding the temperature temporal rate of change. Moreover, the influence of other significant dimensionless parameters on the neutral curve is outlined in Fig. 1. It is observed that an increase in the inverse activation energy notably extends the heating zone in comparison to the cooling zone, particularly evident at higher values, as depicted in Fig. 1b. Similarly, Fig. 1c demonstrates that increments in the inverse dimensionless thermal conductivity expand the heating zone by shifting the linear curve, while the saturation line remains unaffected. Lastly, as illustrated in Fig. 1d, with an increase in the phase change temperature, the linear curve remains unaltered while the saturation line shifts upward, resulting in an expanded cooling zone. Interestingly, these influential parameters alter the neutral curve *only* by modifying its amplitude (or offset) without changing the exponent (or slope) value, thereby resulting in the exponent (slope) value remaining *invariant* in the considered wildfire model.

4 Wildfire Dynamics

4.1 Steady wind velocity: A saddle-type fixed point

We investigate the transient behavior of wildfires within steady wind velocity fields. By utilizing a saddle-type fixed point in the wind velocity topology, characterized by both attraction and repulsion, we analyze the complex dynamics of fire spread, examining how wildfires respond to varying wind patterns across the spatial domain and providing valuable insights into their behavior under diverse conditions. The selected saddle-type wind topology, with stable and unstable eigenvalues of -1 and 1 , is constructed by formulating wind velocity components $u = \xi$ and $v = -\eta$, ensuring the conservation of mass. As depicted in Fig. 2a, the saddle point is located at the origin $(0, 0)$. The stable (repelling) and unstable (attracting) manifolds are also shown. Consistent parameters are used across all simulations to ensure coherence and comparability, including a square domain length of 4, spanning coordinates from -2 to 2 with $\beta = 1$ everywhere across a 256×256 grid. A fixed time step of $\Delta \tau = 10^{-7}$ is used for time integration, and additional parameters include $q = 1$, $\alpha = 10^{-3}$, and $\bar{T}_{pc} = 3$. The initial Heaviside square firefront temperature is uniformly set to

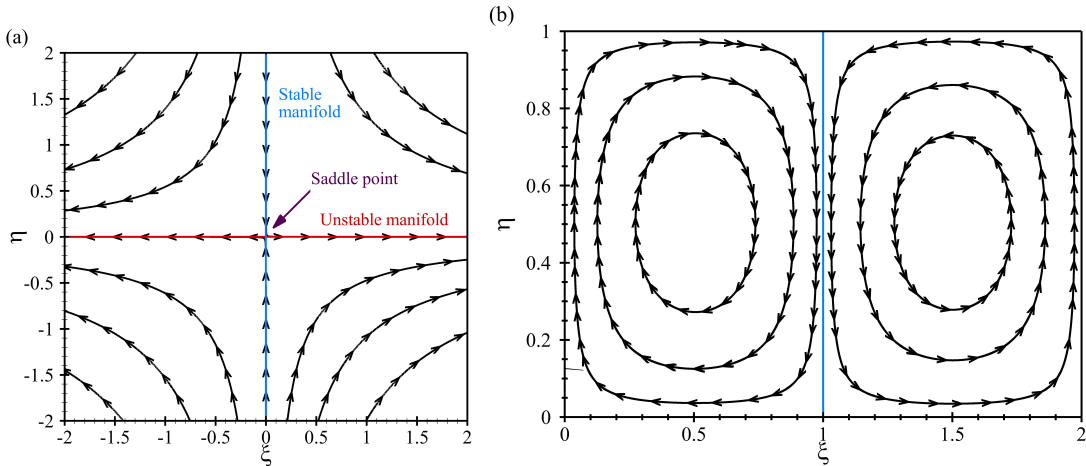


Figure 2: The two wind patterns considered in this study. (a) Steady wind topology showcasing both stable (blue) and unstable (red) manifolds, with a saddle point positioned at the origin, superimposed with velocity streamlines. (b) Unsteady double gyre wind velocity at $\tau = 0$, where the dividing streamline (blue) shows the boundary between the two vortices.

$\bar{T} = 31$, positioned at coordinates $(-1.05, 1.05)$ with a square side length of 0.1, and a normalized maximum wind speed of $|\vec{\mathbf{w}}| = 1$. To maintain consistency across simulations, a stabilization parameter of $C\mu = 0.80$ is used, although this LAD model may not be essential for scenarios with moderate Φ and Da values. To characterize the transient behavior of the initialized firefront, we track the instantaneous locations of four firefronts over time: the top firefront (F_T^Y) advecting along the positive η direction, the bottom firefront (F_B^Y) along the negative η direction, the right firefront (F_R^X) along the positive ξ direction, and the left firefront (F_L^X) along the negative ξ direction. The corresponding group velocities are indicated by V_T^Y , V_B^Y , V_R^X , and V_L^Y , respectively. This tracking method provides a detailed understanding of the firefronts' dynamics and progression under varying convection-diffusion-reaction processes.

4.1.1 Role of Diffusion– Da number

First, we focus on understanding the role of diffusion on the transient behavior of wildfires by varying the Da number across a range of values $(1, 10, 10^2, 10^3)$, while keeping $\Phi = 1.0$ and $\epsilon = 0.03$ constant. The simulation results for $Da = 10^3$ are presented in Fig. 3a, providing insights into the spatio-temporal evolution of the firefront over the uniform fuel bed. At $\tau = 0.15$, the positions of the four tracked firefronts are visually represented by white strips overlaying the fuel bed, progressively advancing along their respective directions over time, while the provided fuel bed undergoes complete gradual consumption, contributing to the fire's progression without being influenced by the manifolds. In the top row of Fig. 3b, the instantaneous positions of these firefronts are depicted for the chosen distinct Da values, indicating the group velocity through their slopes. The group velocity is calculated instantaneously for the given Da and firefronts, followed by temporal averaging. The corresponding temporally averaged group velocities of the firefronts are illustrated in the bottom row of Fig. 3b for different Da values.

Interestingly, the consistent linear progression in the advection of all four firefronts is noted, even as the firefront advances beyond the saddle point in the given wind field. Furthermore, the observed decrease in slope values with increasing Da values across all cases suggests an exponential reduction in group velocity with each increment of Da , eventually converging towards an asymptotic

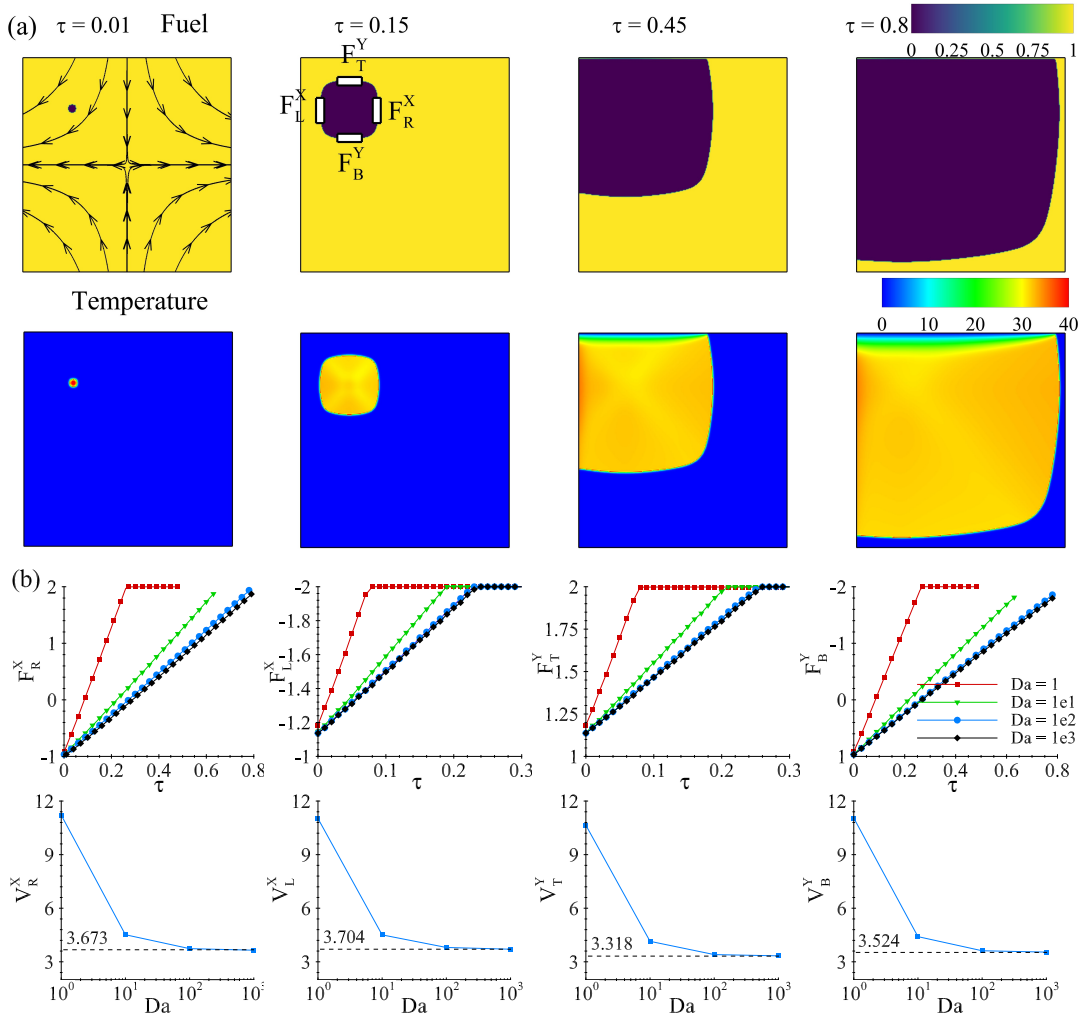


Figure 3: Spatio-temporal evolution of the Heaviside firefront under a saddle-type steady wind velocity field over a uniformly distributed fuel bed, computed across a range of Da values $\in (1, 10, 10^2, 10^3)$, with $\Phi = 1.0$ and $\epsilon = 0.03$. (a) Fuel and temperature fields at various time instants are displayed in the top and bottom rows, respectively, for $Da = 10^3$, with streamlines superimposed at $\tau = 0.01$. At $\tau = 0.15$, the firefront locations are marked by white strips, labeled as the top firefront (F_T^Y), bottom firefront (F_B^Y), right firefront (F_R^X), and left firefront (F_L^X), with superscripts indicating their advection direction. (b) The instantaneous spatial advection of the firefronts and their corresponding time-averaged group velocities are shown, depicted in the top and bottom rows, respectively. The dotted horizontal line represents the asymptotically converged group velocity of the firefronts at an infinite Da number.

value. As a result, an exponential fit regression, expressed as $ae^{bDa} + c$, is employed to quantify the relationship between the firefront's group velocity and the Da number. Here, the coefficients a , b , and c represent the amplitude, the exponential decay of group velocity, and the asymptotically converged group velocity at infinite Da number, respectively. The regression results presented in Table 1 show that the four firefronts converge to distinct asymptotic group velocities, reflecting the influence of the applied wind topology. The results emphasize the significant role of the diffusion process in shaping the transient behavior of wildfires, primarily by modulating the magnitude of their firefront's group velocity while leaving the direction of wildfire propagation unaltered.

Coefficients	Right front	Left front	Top front	Bottom front
a	7.575	7.319	7.329	7.527
b	-0.935	-0.958	-0.947	-0.931
c	3.673	3.704	3.318	3.524

Table 1: Characterizing the time-averaged group velocities of the firefronts for the initialized Heaviside firefront under a saddle-type steady wind velocity field over a uniformly distributed fuel bed, using exponential fitting, for different $Da \in (1, 10, 10^2, 10^3)$, $\Phi = 1.0$, and $\epsilon = 0.03$.

4.1.2 Role of Convection- Φ number

To investigate the influence of convection on wildfire propagation, Φ is varied across values (0.1, 0.05, 0.01), indicative of increasing wind velocity with decreasing Φ . Da number of 10^3 is selected to minimize the diffusion dominance along with $\epsilon = 0.03$. The spatio-temporal evolution of the Heaviside firefront at various time instants is depicted in Fig. 4a, illustrating both the fuel and temperature fields in the top and bottom rows, respectively, computed for $\Phi = 0.05$. A significant departure from the last section arises here, where the observed fuel bed does not undergo complete consumption. Instead, the advection of the firefronts and the corresponding fuel consumption rate are influenced by imposed stable/unstable manifolds. The attracting streamlines propel both the left and right firefronts forward, effectively encouraging complete fuel consumption along their trajectory. Conversely, the repelling streamlines exert a decelerating effect on the top and bottom firefronts, inducing a phenomenon akin to “stalling”, where the fire’s progression is halted, leaving unburnt fuel remnants. This intriguing observation prompts the identification of the spatial location of the stalled top and bottom firefronts, marked by a white dotted curve at $\tau = 0.6$ over the fuel bed in Fig. 4a. Furthermore, at this spatial location, one observes that the convection, diffusion, and reaction contributions balances with each other (the right-hand side of Eq. 16), hence both the temperature temporal rate ($\partial\bar{T}/\partial\tau$) and fuel burn rate ($\partial\beta/\partial\tau$) reach zero. This notable equilibrium delineates the spatial boundary of the stalled firefronts as a “local neutral curve”, beyond which the fire’s progression ceases and cooling gradually occurs over time as all the fuel has been consumed.

From the instantaneous positions of the firefronts, shown in Fig. 4b for different Φ values, one can calculate the exact initial stalling time by identifying when the instantaneous group velocity (local slope) reaches zero before the firefront reaches the domain boundary. For the $\Phi = 0.1$ case, all firefronts advance, consuming all available fuel and reaching the domain boundary, indicating no stalling of firefronts. Conversely, stalling is observed for convection-dominant Φ values of 0.05 and 0.01, even for lower values (results are not shown here). Interestingly, in the case of the lowest chosen Φ value of 0.01, the initialized firefront burns the fuel only in the second quadrant of the domain, primarily through the advection of the left firefront, while the right, top, and bottom firefronts stall despite advancing beyond the saddle fixed point. Stalling here indicates that the front does not reach the boundary. We computed the time-averaged group velocities of the firefronts with the eventual stalled one indicated by a red dot in the bottom row of Fig. 4b. A zero-valued time-averaged group velocity signifies the immediate stalling ($\tau \geq 0$) of firefronts, while the cases that stalled with a non-zero time-averaged group velocity had initial advancements followed by eventual stalling. These discernible insights underscore the substantial impact of the convection process on both the magnitude and direction of the firefront’s group velocity, while the diffusion process, though primarily decreasing its magnitude, exerts a less pronounced influence than convection and does not alter its direction.

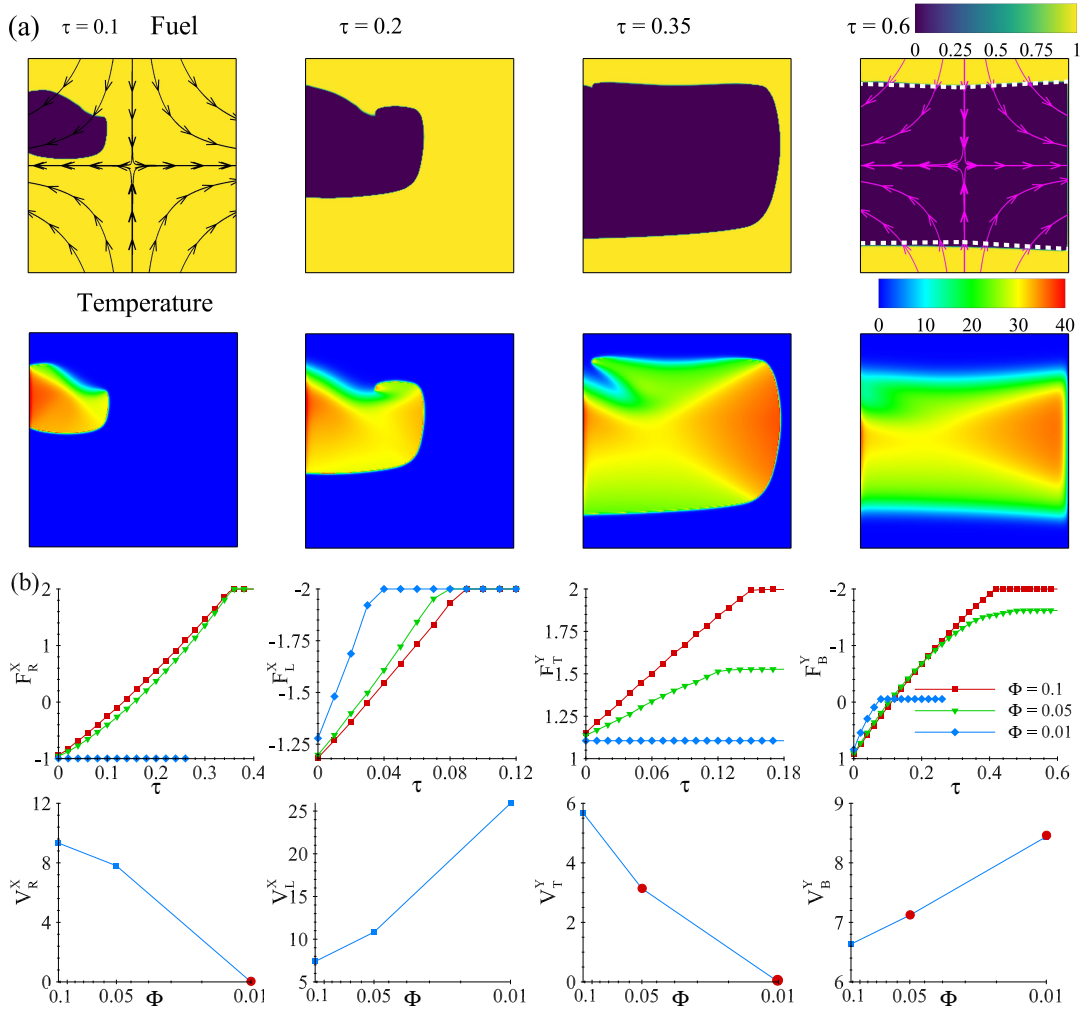


Figure 4: Spatio-temporal evolution of the Heaviside firefront under a saddle-type steady wind velocity field over a uniformly distributed fuel bed, computed across a range of Φ values $\in (0.1, 0.05, 0.01)$, with $Da = 10^3$ and $\epsilon = 0.03$. (a) Fuel and temperature fields at various time instants, with the top and bottom rows, respectively, computed for $\Phi = 0.05$. Streamlines are superimposed at $\tau = 0.1$ and $\tau = 0.6$. At $\tau = 0.60$, the dotted white curve highlights the local neutral curve, indicating the stalled top and bottom firefronts over the fuel bed. (b) Instantaneous spatial advection of the firefronts and their corresponding time-averaged group velocities, depicted in the top and bottom rows, respectively. The red dots highlight the group velocity of stalled firefronts along their respective advecting directions.

4.1.3 Role of Reaction – ϵ parameter

Next, we present how reaction influences transient wildfire behavior by varying ϵ values (0.35, 0.40, 0.45) while selecting a convection-dominant Φ value of 0.05 and ensuring minimal diffusion dominance with Da set to 10^3 . Fig. 5 illustrates the spatio-temporal evolution of the Heaviside firefront at various time instances for $\epsilon = 0.035$, with Fig. 5a showing the fuel and temperature fields in the top and bottom rows, respectively, and Fig. 5b depicting the instantaneous locations of the four advecting firefronts, alongside Fig. 5c, which presents the instantaneous fuel burning rates for the different ϵ values. Similar to the convection-dominated scenarios, the findings depicted in Fig. 5b indicate the stalling of the advecting firefronts in all three ϵ simulation cases, except

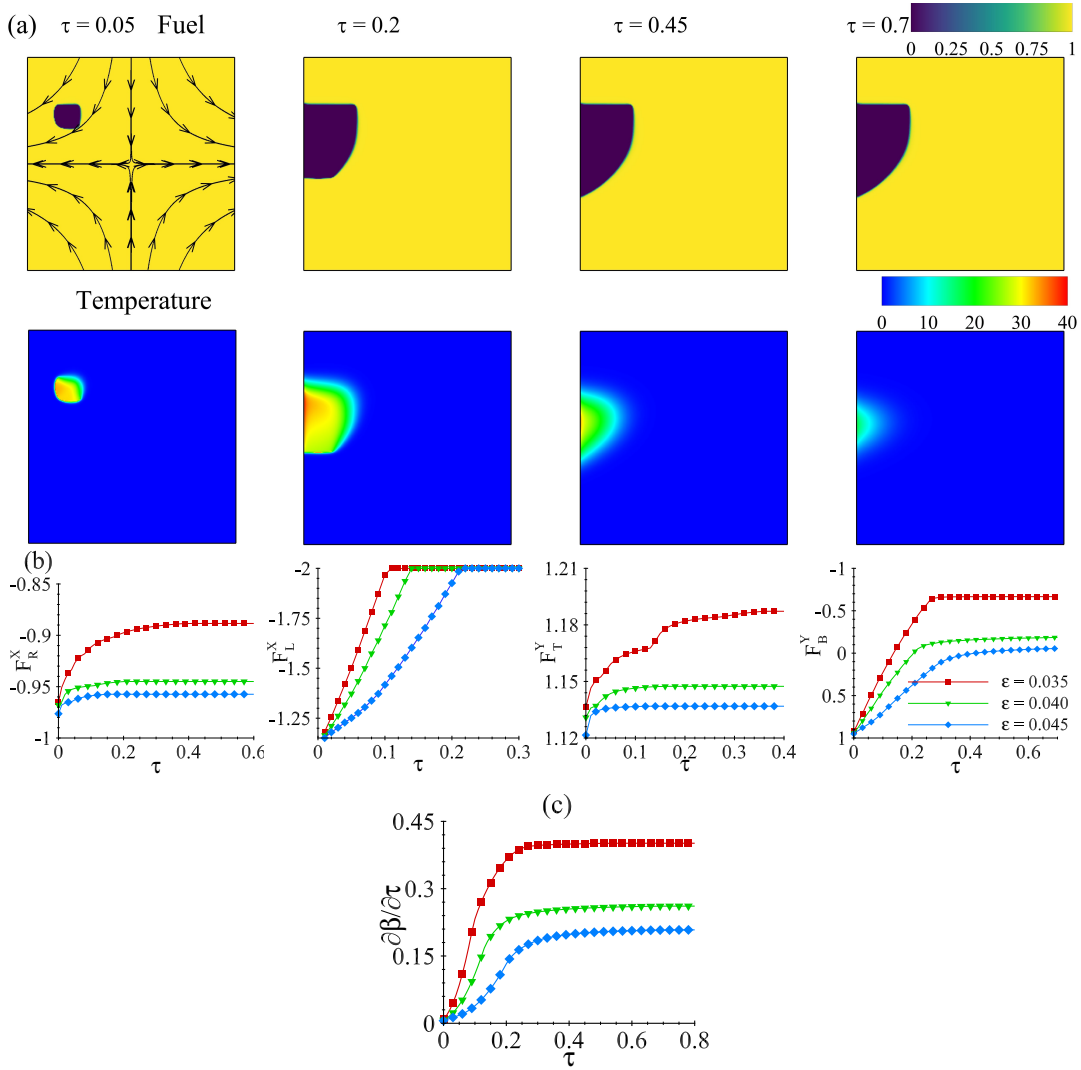


Figure 5: Spatio-temporal evolution of the Heaviside firefront under a saddle-type steady wind velocity field over a uniformly distributed fuel bed, computed across varying ϵ values (0.35, 0.40, 0.45), with $Da = 10^3$ and $\Phi = 0.05$. (a) Fuel and temperature fields at different time instants, with the top and bottom rows corresponding to each field, respectively, calculated for $\epsilon = 0.035$. Streamlines are superimposed at $\tau = 0.05$ over the fuel bed. (b) Instantaneous spatial advection of the four firefronts is plotted. (c) Instantaneous fuel burning rate over time is plotted.

for the left firefront, which is driven by the unstable manifold. In particular, from Eq. 8(a), it is important to recognize the role of ϵ —the reaction parameter—not only in the reaction term but also in the diffusion term, significantly influencing the nonlinearity in the diffusion process. In other words, an increase in ϵ also promotes nonlinear diffusion, consequently resulting in nonlinear propagation of both left and bottom firefronts, with the instantaneous group velocity exhibiting less linear behavior over time, particularly notable in cases with higher ϵ values, as illustrated in Fig. 5b. Moreover, these increments also induce a decelerating effect on the advection of top and right firefronts, reflecting the simplified fuel burning rate formulation (Eq. 1). Further insight from Fig. 5c, illustrating the instantaneous computation of $\partial\beta/\partial\tau$, sheds light on a consistent impediment to the fuel consumption rate due to the decelerated advection of the firefronts, especially as the inverse activation energy (ϵ) increases. We remark that this counter-intuitive observation arises

from the exponential factor present in the reaction term, which is multiplied by ϵ in Eqs. 1 and 16.

4.2 Transient wind velocity: Double gyre flow

We delve into investigating transient wind velocity fields, considering the double gyre flow, a typical benchmark in environmental flows. Double gyre flow is characterized by a pair of two counter-rotating vortices, as shown in Fig. 2b. The double gyre flow is constructed by formulating wind velocity components as

$$u = -A_m \sin(\pi f(\xi, \tau)) \cos(\pi \eta) \quad (17a)$$

$$v = A_m \cos(\pi f(\xi, \tau)) \sin(\pi \eta) \frac{df}{d\xi} \quad (17b)$$

where $f(\xi, \tau) = \lambda \sin(2\pi\Omega\tau)\xi^2 + [1 - 2\lambda \sin(2\pi\Omega\tau)]\xi$, with λ the perturbation amplitude representing how far the dividing streamline perturbs from the initial position, Ω the oscillation frequency indicating the rate of this perturbation, and A_m the velocity magnitude. The wind oscillation frequency, normalized by the total fuel consumption timescale \bar{t}_r (the time required to completely burn all the given fuel), is represented by the Strouhal number $St = \bar{t}_r\Omega$, quantifying the interaction between fuel reaction and flow oscillation timescales. Consistent parameters across simulations include a rectangular domain of 2×1 along the ξ and η axes, a 256×128 grid, $\beta = 1$, a time step of $\Delta\tau = 10^{-8}$, $q = 1$, $\alpha = 10^{-3}$, $\bar{T}_{pc} = 3$, and an initial Heaviside square firefront temperature $\bar{T} = 31$ at $(1.0, 0.5)$ with a side length of 0.1 along the dividing streamline. Simulations employ a normalized maximum wind speed $|\vec{w}| = 1$ and LAD coefficient $C\mu = 0.75$ to examine transient wildfire dynamics under convection-dominant and low-diffusion scenarios, defined by $\Phi = 10^{-3}$, $Da = 10^3$, and $\epsilon = 0.03$. Given the transient wind topology, instantaneous FTLE fields were computed both forward and backward in time over an integration period of 20, allowing for the extraction of repelling and attracting Lagrangian coherent structures (rLCS and aLCS) at a given time τ .

4.2.1 Role of wind oscillation - St Number

To effectively investigate the interaction between transient wildfires and time-varying wind topology, we select a wind oscillation timescale ($1/\Omega$) that aligns with the total fuel reaction timescale \bar{t}_r . A transient wildfire simulation with a steady double-gyre wind velocity ($\Omega = 0$) determined the fuel consumption timescale $\bar{t}_r \sim 10^{-2}$. Consequently, we select the wind oscillation frequency to be on the order of \bar{t}_r . In Fig. 6, the spatio-temporal evolution of the Heaviside firefront at various time instants is presented under an unsteady double-gyre wind flow, oscillating at a frequency of $St = 2$, with an oscillation amplitude of $\lambda = 0.25$ and a velocity magnitude of $A_m = 0.1$. Figure 6a illustrates the fuel and temperature fields along with the corresponding instantaneous rLCS and aLCS results. At $\tau = 0.001$, the initialized Heaviside firefront is advected left, right, and downward, resulting in three distinct firefronts—the left firefront F_{L1}^X , the right firefront F_{R1}^X , and the bottom firefront F_B^Y —with dotted lines indicating their locations within the temperature field. Upon examining the fuel bed traces, it becomes evident that the left firefront advances considerably further than the right firefront. This is attributed to the influence of the aLCS-1, which specifically drives the advection of the left firefront while exerting no effect on the right firefront. In contrast, the right firefront experiences moderated advection due to the presence of rLCS-2, which repels and decelerates its progression. Although aLCS-2 is anticipated to contribute to the advancement of the right firefront, its influence is diminished by the preceding rLCS-2, which constrains the progress of the right firefront. This deceleration effect is most pronounced while rLCS-2 remains in

the upstream region of the right firefront. However, since wildfire transport is not a pure advection problem and LCS cannot form transport barriers, ultimately, the firefront passes rLCS-2, and aLCS-2 begins to accelerate the advection of the right firefront, as observed at $\tau = 0.0025$. The deceleration action exerted by rLCS-2 is distinctly evident in the tracked instantaneous location plot of F_{R1}^X , illustrated in Fig. 6b, where the red box highlights a notable reduction in the instantaneous firefront's group velocity, followed by a subsequent increment corresponding to the traversal of rLCS-2. This differential behavior emphasizes the contrasting roles of aLCS-2 and rLCS-2 in shaping the firefront dynamics. Moreover, the bottom firefront does not advance uniformly downward but is distorted due to the decelerating influence of rLCS-1, as evidenced by the non-parallel alignment of the identified dotted line in the temperature field.

At $\tau = 0.0025$, two additional distinct top firefronts appear alongside the existing right and left firefronts. These newly identified top firefronts are designated as F_{T1}^Y and F_{T2}^Y within the temperature field, resulting from the advection of the left and right firefronts, respectively. It is observed that the advected distances of these two top firefronts differ, revealing an asymmetry in their advection. This asymmetry is attributable to the repelling influence over F_{T2}^Y firefront by rLCS-2, which precedes the aLCS-2 curve. This phenomenon mirrors the disparity observed between the right and left firefronts at the earlier time $\tau = 0.001$. In addition, the other three firefronts F_{L1}^X and F_{T1}^Y are attracted by the aLCS-1, while F_{R1}^X is attracted by aLCS-2 curve, leading to more effective progression without noticeable deceleration. By $\tau = 0.0035$, the accelerating influence of highlighted aLCS curves on the firefronts F_{L1}^X , F_{R1}^X , and F_{T2}^Y becomes more pronounced, effectively overshadowing the decelerative effects of the corresponding rLCS curves, allowing each firefront to advance along its respective trajectory. Interestingly, F_{T1}^Y progresses primarily due to diffusion, as neither aLCS nor rLCS exert any significant influence in this region. At a later time $\tau = 0.005$, the continued advection of the two top firefronts gives rise to the emergence of additional left and right firefronts, which are labeled F_{L2}^X and F_{R2}^X , respectively. In this scenario, all four identified firefronts experience progressive advection, guided by the attractive influence of the highlighted aLCS curves. It is particularly noteworthy that the highlighted rLCS curves exert no significant influence on the firefronts during this phase. A similar advection scenario is observed at $\tau = 0.0065$, where the firefronts continue to be effectively attracted by the highlighted aLCS curves. The asymmetry between the left firefront F_{L2}^X and the right firefront F_{R2}^X reflects the earlier asymmetry observed in the earlier case of F_{T1}^Y and F_{T2}^Y firefronts, which, in turn, stems from the differential advection of F_{L1}^X and F_{R1}^X . In Fig. 6b, the instantaneous advection of the four firefronts is depicted to quantify its spatio-temporal characteristics in relation to the influence of aLCS and rLCS fields over time τ . Among the four cases presented, only the right firefront demonstrates a noticeable nonlinear instantaneous group velocity due to the traversal of the rLCS across it, while the other firefronts experience progressive advancement throughout time. The observed asymmetry in the firefronts' advancement is quantitatively reflected in the propagation times shown in the corresponding plots. That is, the left firefront advects faster than the right one ($t_{left} < t_{right}$), and a similar trend is observed in the other two top firefronts. Further quantitative analysis of this asymmetry will be discussed in the subsequent section.

Next, the transient behavior of wildfires is investigated under an unsteady double gyre flow oscillating at a high frequency, characterized by a Strouhal number $St = 7.5$, employing the same other parameters, including an oscillation amplitude of $\lambda = 0.25$ and a velocity magnitude of $A_m = 0.1$. This case aims to elucidate the wildfire dynamics when the time scales of fuel consumption and wind flow oscillation are disparate. Figure 7 illustrates the spatio-temporal evolution of the Heaviside firefront under the considered unsteady double gyre flow scenario. As anticipated, the advection of all firefronts nearly exhibits symmetric advancement across the fuel bed, since the

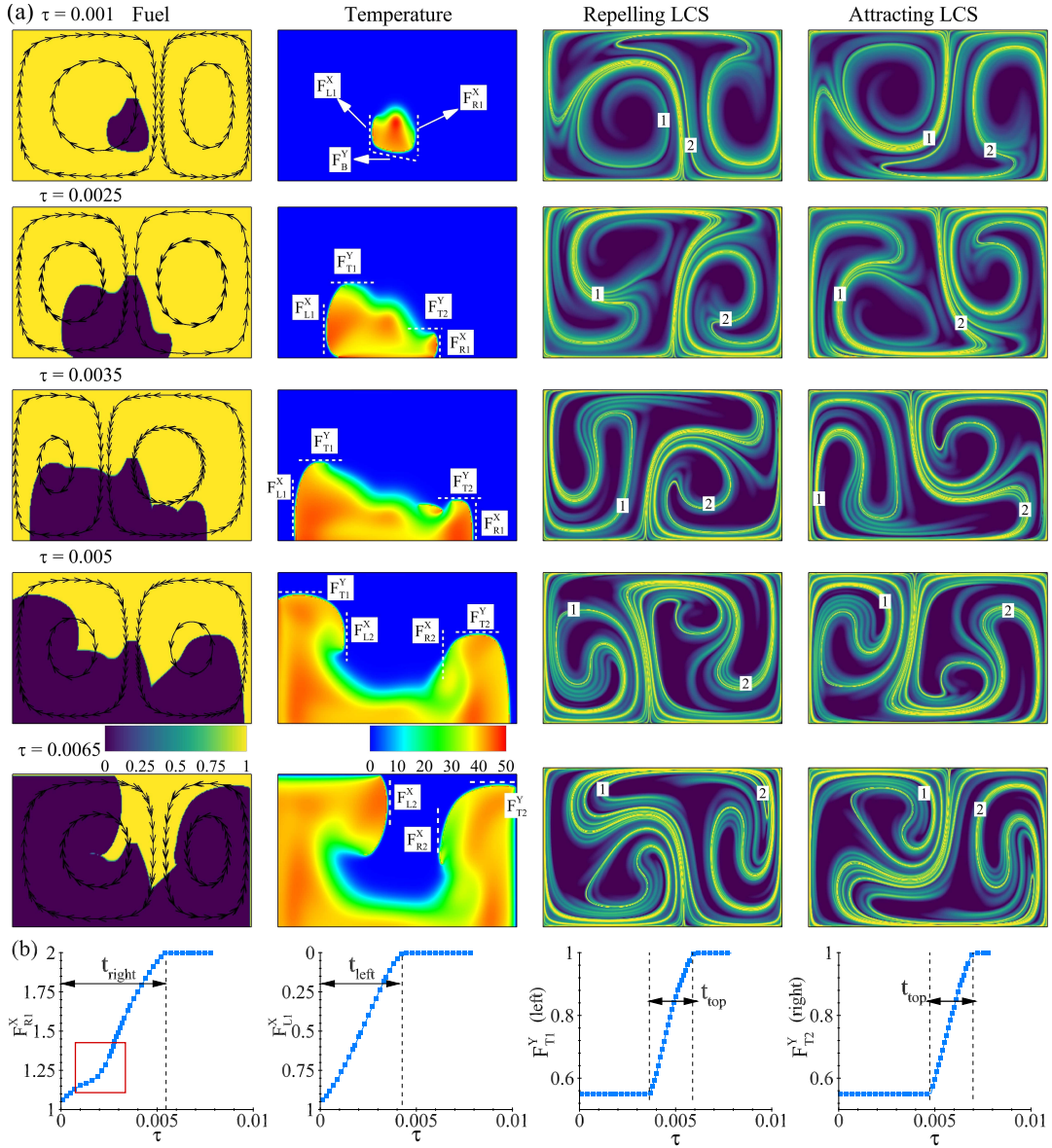


Figure 6: Spatio-temporal evolution of the Heaviside firefront under a double gyre wind velocity field, characterized by parameters $A_m = 0.1$, $St = 2$, and $\lambda = 0.25$, over a uniformly distributed fuel bed, computed at $\Phi = 10^{-3}$, $Da = 10^3$, and $\epsilon = 0.03$. (a) The fuel and temperature fields are shown at various time instants, accompanied by the corresponding repelling and attracting LCS plots, with streamlines superimposed over the fuel bed. (b) The instantaneous spatial advection of the four firefronts is plotted.

flow oscillation time is considerably smaller than the fuel consumption time scale, implying that the firefronts do not have sufficient time to respond to the wind oscillations. Consequently, the subsequent emergence of top firefronts (resulting from the advection of right/left firefronts) also displays a nearly symmetric advection. The instantaneous locations of the tracked firefronts, as depicted in Fig. 7a, further substantiate this nearly symmetric advection ($t_{left} \approx t_{right}$) over the evolution time τ . Although changes in local group velocity for both the right and left firefronts are evident, as highlighted within the red box panel, the local deceleration/acceleration is minimal compared to the last transient case. The instantaneous FTLE fields and corresponding aLCS and

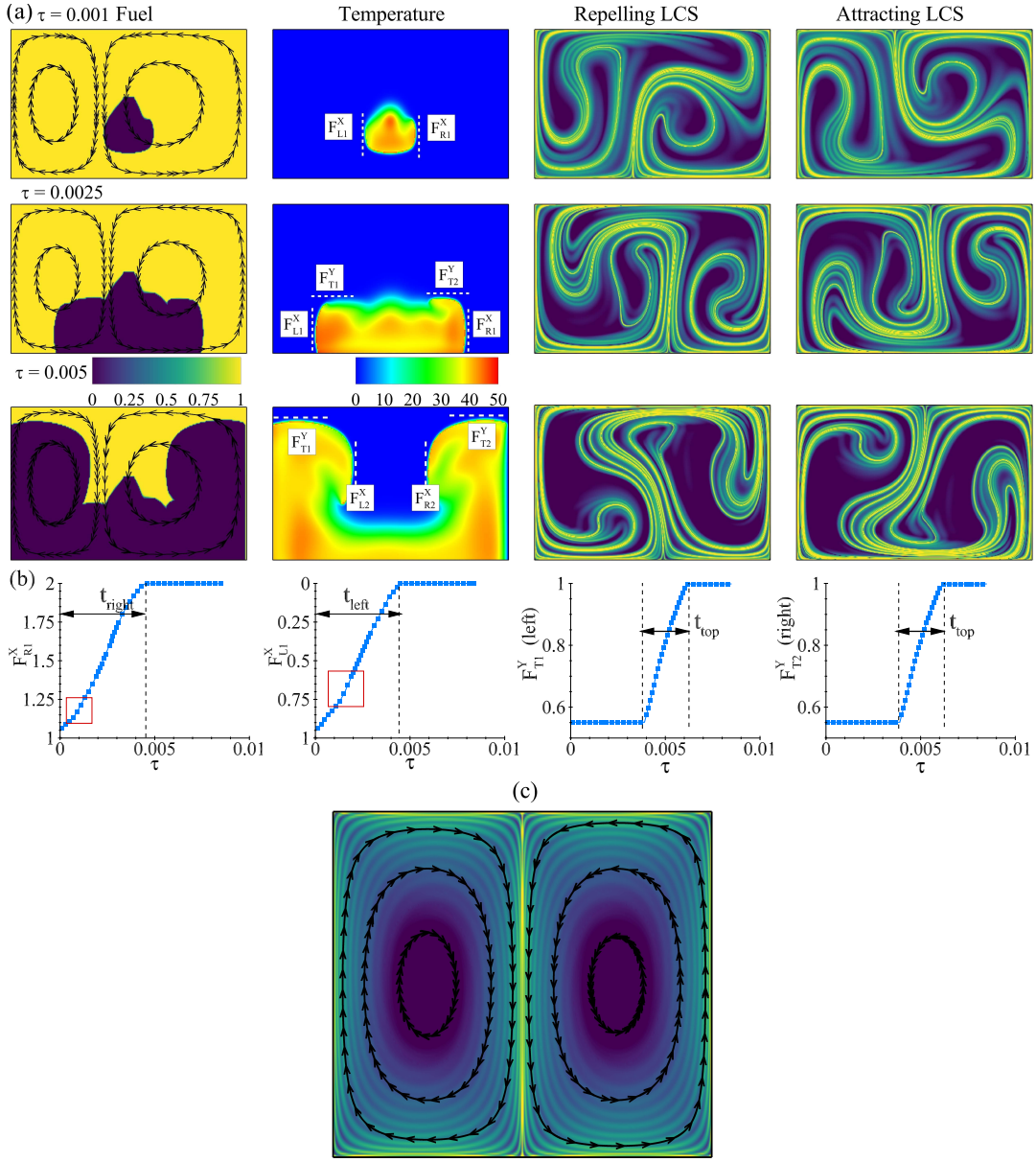


Figure 7: Spatio-temporal evolution of the Heaviside firefront under a double gyre wind velocity field, characterized by parameters $A_m = 0.1$, $St = 7.5$, and $\lambda = 0.25$, over a uniformly distributed fuel bed, computed at $\Phi = 10^{-3}$, $Da = 10^3$, and $\epsilon = 0.03$. (a) The fuel and temperature fields at various time instants, along with the corresponding repelling and attracting LCS plots, with streamlines superimposed over the fuel bed. (b) The instantaneous spatial advection of the four firefronts is plotted. (c) The FTLE field corresponding to the time-averaged wind velocity fields superimposed with time-averaged streamlines.

rLCS reveal an asymmetric pattern, which appears to be unrelated to the high-Strouhal number oscillation scenario. Instead, FTLE calculation on the time-averaged wind velocity field, as shown in Fig. 7c is sufficient to characterize the advection of firefronts in this case. Notably, the LCS manifests as a ridge-like structure along the dividing streamline. In the present case, all firefronts adhere to the time-averaged local streamlines, much like the behavior observed in a saddle-type steady wind velocity scenario.

By comparing two Strouhal number cases, it becomes evident that asymmetric advection of

firefronts is more pronounced when $St = 2$, where wind oscillation closely aligns with the fuel consumption time scale. In contrast, minimal asymmetry is observed when $St = 7.5$, where the respective time scales are misaligned, indicating that the degree of asymmetry is most notable when $St \rightarrow 1$. To address this quantitatively, one can project the advection characteristics of the firefronts onto a Bode plot—similar to the approach used by Ducruix et al. (2000) for transient premixed flames—thereby providing a comprehensive understanding of the wildfire’s response to unsteady wind conditions.

4.2.2 Dynamic response of wildfires to unsteady wind oscillation

The dynamic response of wildfires to the imposed unsteady double-gyre wind topology is systematically quantified by projecting their advection characteristics onto a Bode plot through a transfer function approach. In the Bode plot, a transfer function (TF) is generally defined as $TF = \bar{R}\angle\phi$, where magnitude (\bar{R}) denotes the magnitude gain, and the phase angle (ϕ) indicates the phase difference of an output and an input response.

Transfer function of the right firefront (TF_R) is given by

$$TF_R = \bar{R}_R \angle \phi_R ; \quad \begin{cases} \bar{R}_R = \frac{V_R^X}{V_L^X} \\ \phi_R = \left[\frac{t_{right}}{t_{right}|_{St=0}} - 1 \right] \pi . \end{cases} \quad (18)$$

Similarly, the transfer function of the left firefront (TF_L) is given by

$$TF_L = \bar{R}_L \angle \phi_L ; \quad \begin{cases} \bar{R}_L = \frac{V_L^X}{V_R^X} = \frac{1}{\bar{R}_R} \\ \phi_L = \left[\frac{t_{left}}{t_{left}|_{St=0}} - 1 \right] \pi . \end{cases} \quad (19)$$

It is important to note that the magnitude of the TF quantifies the degree of asymmetry between the advection of the right and left firefronts by calculating their time-averaged group velocity, thereby reflecting the uneven spread of the fire under the influence of the unsteady double-gyre wind. A TF magnitude different from unity indicates asymmetric transport, suggesting that similar asymmetry should be observed in the advection of subsequent formations of other top firefronts, as discussed earlier. Additionally, the phase angle of the TF shows the phase response of the firefronts relative to a baseline scenario characterized by a steady wind topology ($St = 0$), where a negative phase angle indicates a phase lag and a positive phase angle denotes a phase advance in the response of the firefront progression to wind oscillation. Figure 8 presents the Bode plot illustrating the transient wildfire characteristics of firefronts subjected to an unsteady double gyre flow, demonstrating the transfer function of both right and left firefronts across varying Strouhal numbers and oscillation amplitudes, $\lambda \in (0.05, 0.15, 0.25)$. The \bar{R}_L plot is omitted as it is the inverse of \bar{R}_R . Notably, the phase response of both firefronts is not monotonous, reaching zero for certain Strouhal numbers, which indicates the existence of a *phase inversion frequency* in the transient wildfire propagation scenario under unsteady wind conditions, implying a phase-switching phenomenon where the fire response shifts from advance to lag or vice versa, as similarly observed in Motta et al. (2015); Viknesh and Poddar (2021) for unsteady flow control applications.

From Fig. 8a, it is evident that for any given oscillation amplitude λ , the \bar{R}_R value of the right firefront exhibits a significant deviation from unity and a resonance condition when $1 \lesssim St \lesssim 4$.

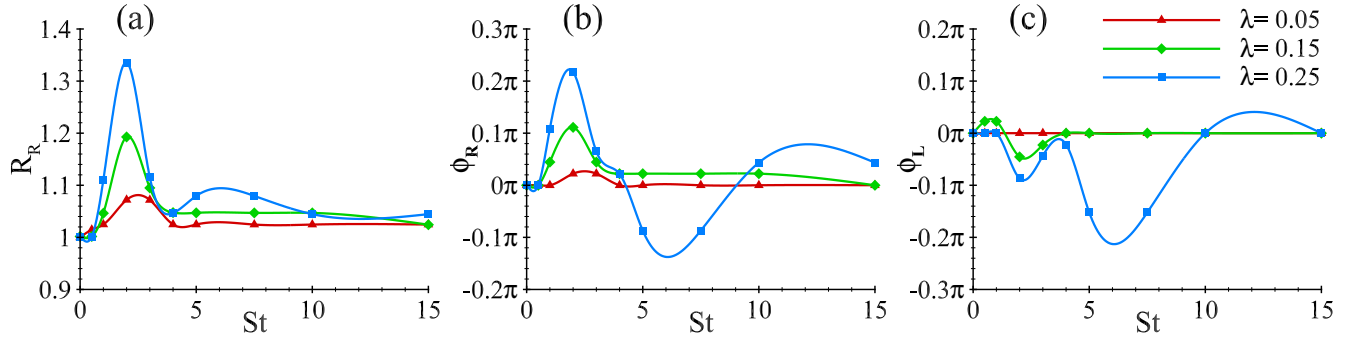


Figure 8: Bode plots – (a) The magnitude of the TF_R , (b) the phase angle of the TF for the right firefront, and (c) the phase angle of the TF for the left firefront are shown. These results are computed with $A_m = 0.1$, $\Phi = 10^{-3}$, $Da = 10^3$, and $\epsilon = 0.03$ for different wind oscillation amplitudes (λ) and Strouhal numbers.

Conversely, for small Strouhal numbers and oscillation amplitudes λ , \bar{R}_R approaches unity, signifying that the effect of wind unsteadiness diminishes. In contrast, for very large Strouhal numbers, the firefront has insufficient time to effectively respond to the oscillations, resulting in \bar{R}_R remaining close to unity with minimal deviation due to the rapid oscillations. Examination of the real part of the transfer function (TF_R) in the Bode plot reveals that, under resonance conditions with moderate Strouhal numbers, instantaneous FTLE calculations are essential for precise prediction of wildfire dynamics. Conversely, when the Strouhal number is significantly greater than one ($St \gg 1$) and oscillation amplitudes are small ($\lambda \ll 1$), FTLE values based on time-averaged wind velocity are adequate for forecasting wildfire behavior across the fuel bed.

5 Conclusion

In the present research, the wildfire transport model proposed by Asensio and Ferragut (2002) has been employed to study the role of flow topology under two benchmark wind flow typologies: steady wind with saddle-type fixed points and unsteady wind characterized by double gyre flow. The key outcomes of this study are enumerated as follows:

(a) The wildfire combustion model has been revisited and non-dimensionalized by introducing three distinct time scales that define the convection-diffusion-reaction process. This revision led to the identification of two non-dimensional numbers: the Damköhler number (Da) and a newly defined non-dimensional number (Φ), representing the ratio of the Damköhler number to the Peclet number. This approach contrasts with the conventional non-dimensionalization, which typically incorporates a single time scale, thereby culminating in a revised new non-dimensional wildfire combustion model with additional physical insight.

(b) Through scaling analysis, critical determinants of transient wildfire behavior were identified, including the state-neutral curve where the temporal rate of fire temperature is zero for specific combinations of the two non-dimensional numbers. This finding offers a valuable tool for predicting overall wildfire dynamics from initial conditions, thus mitigating the reliance on extensive and computationally intensive simulations.

(c) A robust wildfire transport solver has been developed, leveraging CUDA support within a finite difference method framework. The solver employs compact schemes and implicit-explicit Runge-Kutta methods to resolve both spatial and temporal solutions while incorporating the LAD

model to selectively attenuate high-frequency instabilities without compromising accuracy in smooth regions.

(d) In the steady saddle-type fixed point wind topology, it was demonstrated that the unstable manifold (attracting LCS) significantly influences firefronts, guiding them along their trajectory. Conversely, the stable manifold (repelling LCS) exerts a decelerating influence, causing the firefronts to stall and inhibiting further propagation, particularly under conditions characterized by a large Da and a small Φ , where convection predominates, and diffusion is minimal. However, due to the simplified fuel reaction composition in the Asensio and Ferragut (2002) model, definitive conclusions regarding the reaction component's interaction with both stable and unstable manifolds remain to be investigated in detail.

(e) In the context of unsteady double gyre flow, the investigation illustrated that instantaneous FTLE fields—comprising unstable and stable manifolds—are pivotal in governing the advection of firefronts at moderate Strouhal numbers, particularly when resonance occurs with wildfire–wind oscillations. In contrast, at very high Strouhal numbers, where off-resonance conditions prevail, wildfire propagation is more strongly influenced by time-averaged FTLE fields. By projecting the advection characteristics of firefronts onto a Bode plot, it becomes possible to determine the conditions under which either the instantaneous or time-averaged FTLE should be computed for more accurate predictions of wildfire propagation. Furthermore, the existence of *phase inversion frequency* (Strouhal number) has been identified for wildfire propagation when subjected to transient wind conditions.

Future research should focus on several key areas to advance our understanding of wildfire dynamics. Incorporating realistic vegetation distributions, including firebreaks, along with two-way coupled wind velocity computations using the Navier-Stokes equations and wildfire equations, will provide a more nuanced perspective on wind–fire interactions. Additionally, integrating actual terrain topography, including both uphill and downhill scenarios, is crucial for accurately capturing the effects of terrain on wildfire behavior. Examining the relevance of LCS within these more complex and realistic settings will enhance predictive models and deepen our comprehension of complex wildfire propagation patterns.

Acknowledgment

We gratefully acknowledge the NSF EAGER grant (Award No. 2330212) from the Combustion and Fire Systems program. Additionally, co-author AT would like to acknowledge partial support from the Industry Advisory Board of the NSF-IUCRC Wildfire Interdisciplinary Research Center (WIRC) at San José State University (Award No. 2113931).

Declaration of Interests

The authors report no conflict of interest.

Data availability

The developed wildfire transport python solver will be available on GitHub after peer review.

A Implicit-Explicit time integration algorithm

IMEX-RK scheme for the new wildfire model

Initial solution \mathbf{T}^n and β^n at $\tau = \tau^n$

do $i = 1, \dots, s$

compute the stage values: $2 \leq i \leq s$

$$\widehat{\mathbf{T}}^{(i)} \leftarrow \mathbf{T}^n + \Delta\tau \sum_{j=1}^{i-1} \tilde{a}_{ij} F_j^T, \quad \overline{\mathbf{T}}^{(i)} \leftarrow \mathbf{T}^n + \Delta\tau \sum_{j=1}^{i-1} a_{ij} F_j^T, \quad \beta^{(i)} \leftarrow \beta^n + \Delta\tau \sum_{j=1}^{i-1} a_{ij} F_j^\beta$$

compute

$$F_i^\beta \leftarrow -\frac{\epsilon}{q} \frac{\beta^{(i)} s(\widehat{\mathbf{T}}^{(i)}) + e^{\widehat{\mathbf{T}}^{(i)}/(1+\epsilon\widehat{\mathbf{T}}^{(i)})}}{[1 + (\epsilon/q) \Delta\tau a_{ii} s(\widehat{\mathbf{T}}^{(i)}) + e^{\widehat{\mathbf{T}}^{(i)}/(1+\epsilon\widehat{\mathbf{T}}^{(i)})}]}$$

solve for F_i^T the linear system:

$$F_i^T = \frac{1}{Da} \nabla \cdot [K(\widehat{\mathbf{T}}^{(i)}) \nabla(\overline{\mathbf{T}}^{(i)} + \Delta\tau a_{ii} F_i^T)] + s(\widehat{\mathbf{T}}^{(i)}) + [\beta^{(i)} + \Delta\tau a_{ii} F_i^\beta] e^{\widehat{\mathbf{T}}^{(i)}/(1+\epsilon\widehat{\mathbf{T}}^{(i)})} \\ - \alpha[\overline{\mathbf{T}}^{(i)} + \Delta\tau a_{ii} F_i^T] - \frac{\vec{\mathbf{w}}}{\Phi} \cdot \nabla \widehat{\mathbf{T}}^{(i)} + \Delta_T^2(\widehat{\mathbf{T}}^{(i)})$$

end do

$$\mathbf{T}^{n+1} \leftarrow \mathbf{T}^n + \Delta\tau \sum_{j=1}^s b_j F_j^T, \quad \beta^{n+1} \leftarrow \beta^n + \Delta\tau \sum_{j=1}^s b_j F_j^\beta$$

Marched solution: \mathbf{T}^{n+1} and β^{n+1} at $\tau^{n+1} = \tau^n + \Delta\tau$

Here, a_{ij} and \tilde{a}_{ij} represent the coefficients in a standard Butcher tableau, used to calculate internal temporal stages performing simultaneous explicit and implicit time integration in an IMEX-RK scheme setting.

B Numerical solver validation

In this section, we validate our solver using a benchmark 2D perfect initial Heaviside firefront over a uniform fuel distribution scenario, as presented in Bürger et al. (2020). Resolving the advecting Heaviside firefront over a long integration time poses a significant numerical challenge, as it excites all possible frequencies, including spurious ones associated with Gibbs' oscillation in a Fourier spectrum. Despite this challenge, the OUCS2 compact scheme adeptly captures the spatiotemporal evolution of the Heaviside firefront effectively, even *without* incorporating the LAD model for the considered wildfire scenario (Fig. 9). We maintain consistency by adhering to the parameters in Bürger et al. (2020): a square domain size of $l_0 = 50$, $\epsilon = 3 \times 10^{-2}$, $q = 1$, $\alpha = 10^{-3}$, $\overline{T}_{pc} = 3$, initial firefront temperature $\overline{T} = 31$, wind speed $|\vec{\mathbf{w}}| = 425$ with a direction of 45° , $C_\mu = 0$, and $Da = \Phi = 1$. Furthermore, with the initial firefront precisely positioned at coordinates (8.0, 8.0) and a square side length of 4, and the fuel uniformly initialized at 0.6 across the spatial domain, the simulation is conducted with a time step of $\Delta\tau = 10^{-7}$ over a grid size of 256×256 . The results

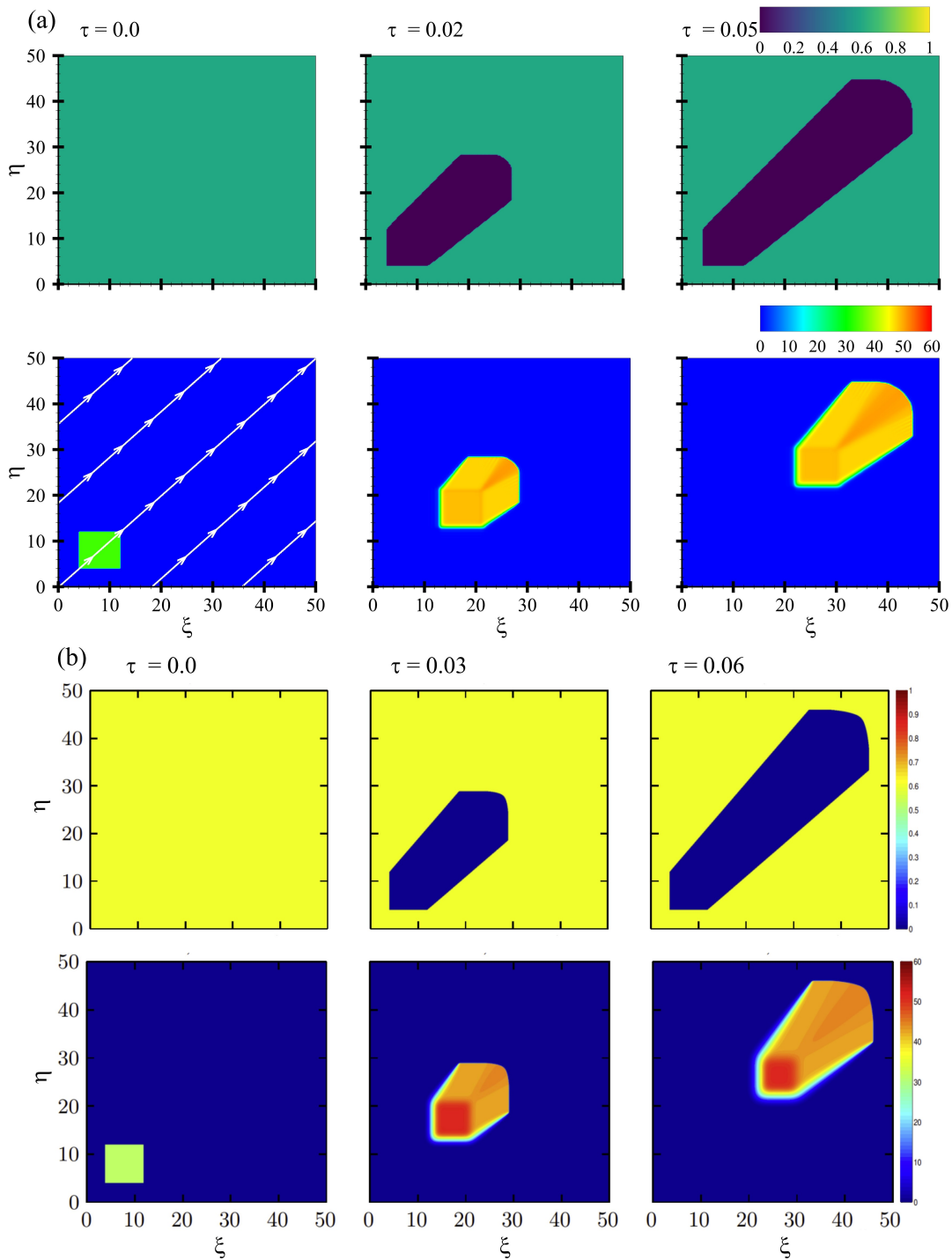


Figure 9: Comparison of the spatio-temporal evolution of the Heaviside firefront over uniformly distributed fuel, (a) computed using our FDM solver and compared against (b) results from (Bürger et al., 2020). Both fuel and temperature distributions are depicted at various time instants in the top and bottom rows, respectively. Panel (b) in the figure adapted from Bürger et al. (2020) with permission. Copyright MDPI 2020.

depicted in Fig. 9, illustrate the spatio-temporal evolution of the Heaviside firefront at different time instants, demonstrating good agreement with the Bürger et al. (2020) results. Discrepancies may arise from using a more accurate IMEX-RK3 time integration and OUCS2 schemes in our work,

contrasting with the employment of IMEX-RK2 scheme and highly dissipative WENO scheme in Bürger et al. (2020).

C Notations

Notation	Definition
A	pre-exponential factor
E_A	activation energy
R	universal gas constant
T	absolute temperature
r	reaction rate
Y	mass fraction of fuel
ρ	density of air
\vec{v}	velocity vector
U_∞	maximum freestream velocity magnitude
T_∞	absolute ambient temperature
σ	Stefan-Boltzmann constant
δ	optical path length for radiation
h	natural convection coefficient
H	heat of combustion
k	thermal conductivity of fluid
C	specific heat of fluid
q	non-dimensional reaction heat
t_0	characteristic temporal scale
t_d	characteristic diffusion time scale
t_r	characteristic fuel reaction time scale
t_f	characteristic flow advection time scale
l_0	characteristic spatial scale
\vec{w}	normalized velocity vector
ϵ	inverse activation energy at T_∞
Y_0	initial mass fraction of fuel
β	normalized mass fraction of fuel
β_{max}	initial normalized mass fraction of fuel

Continued on next page

Table 2 – continued from previous page

Notation	Definition
\hat{n}	unit normal vector
∇	gradient operator
T_{pc}	phase change temperature
$s(T)^+$	phase change function
α	non-dimensional natural convection coefficient
$\bar{\kappa}$	inverse non-dimensional conductivity coefficient
\bar{T}	non-dimensional absolute temperature
\bar{T}_{max}	maximum non-dimensional absolute temperature
\bar{T}_{pc}	non-dimensional phase change temperature
$s(\bar{T})^+$	non-dimensional phase change function
Da	Damköhler number
Pe	Peclet number
Φ	Ratio of Damköhler number to Peclet number
h_x	spatial grid spacing
\hat{T}	non-stiff \bar{T}
τ	dimensionless evolution time
τ^n	current temporal solution
τ^{n+1}	future temporal solution
$\Delta\tau$	temporal resolution
Δ_T^2	localized artificial diffusion
μ	localized artificial diffusion coefficient
C_μ	localized artificial diffusion magnitude
$\mathbf{H}_{\mathbf{F}}$	Heaviside function for locating discontinuities
$\hat{\mathbf{C}}$	Cauchy-Green Strain tensor
\hat{t}_0	Initial time for computing FTLE integration
t_1	FTLE integration time period
$\hat{\sigma}$	FTLE field
\bar{h}_x	firefront thickness
x, y	spatial coordinates
ξ, η	normalized spatial coordinates

Continued on next page

Table 2 – continued from previous page

Notation	Definition
u, v	wind velocity components along ξ and η axis
F_T^Y	top firefront advecting along $-\eta$ direction
F_B^Y	bottom firefront advecting along $+\eta$ direction
F_R^X	right firefront advecting along $+\xi$ direction
F_L^X	left firefront advecting along $-\xi$ direction
V_T^Y	Time-averaged group velocity of top firefront
V_B^Y	Time-averaged group velocity of bottom firefront
V_R^X	Time-averaged group velocity of right firefront
V_L^X	Time-averaged group velocity of left firefront
A_m	Velocity magnitude
λ	Wind oscillation amplitude
Ω	Wind oscillation frequency
\bar{t}_r	Total fuel consumption time scale
St	Strouhal number
t_{left}	Time taken by F_L^X to reach the left boundary
t_{right}	Time taken by F_R^X to reach the right boundary
t_{top}	Time taken by F_T^Y to reach the top boundary
TF	Transfer function
\bar{R}, ϕ	Real and phase angle of TF
\bar{R}_R, ϕ_R	Real and phase angle of TF for a right firefront
\bar{R}_L, ϕ_L	Real and phase angle of TF for a left firefront

Table 2: Nomenclature of parameters used in the wildfire combustion model.

References

- D. R. Allen, M. D. Fromm, G. P. Kablick III, G. E. Nedoluha, and D. A. Peterson. Smoke with induced rotation and lofting (swirl) generated by the february 2009 australian black saturday pyrocb plume. *Journal of Geophysical Research: Atmospheres*, 129(5), 2024.
- M. R. Allshouse and T. Peacock. Lagrangian based methods for coherent structure detection. *Chaos: An Interdisciplinary Journal of Nonlinear Science*, 25(9), 2015.
- E. Amini, M. S. Safdari, D. R. Weise, and T. H. Fletcher. Pyrolysis kinetics of live and dead wildland vegetation from the southern united states. *Journal of Analytical and Applied Pyrolysis*, 142:104613, 2019.

- A. Arzani and S. C. Shadden. Characterization of the transport topology in patient-specific abdominal aortic aneurysm models. *Physics of Fluids*, 24(8):1901, 2012.
- M. I. Asensio and L. Ferragut. On a wildland fire model with radiation. *International Journal for Numerical Methods in Engineering*, 54(1):137–157, 2002.
- M. Aslani and J. D. Regele. A localized artificial diffusivity method to simulate compressible multiphase flows using the stiffened gas equation of state. *International Journal for Numerical Methods in Fluids*, 88(9):413–433, 2018.
- A. L. Atchley, R. Linn, A. Jonko, C. Hoffman, J. D. Hyman, F. Pimont, C. Sieg, and R. S. Middleton. Effects of fuel spatial distribution on wildland fire behaviour. *International journal of wildland fire*, 30(3):179–189, 2021.
- P. Babak, A. Bourlioux, and T. Hillen. The effect of wind on the propagation of an idealized forest fire. *SIAM Journal on Applied Mathematics*, 70(4):1364–1388, 2009.
- S. Balasuriya, N. T. Ouellette, and I. I. Rypina. Generalized Lagrangian coherent structures. *Physica D: Nonlinear Phenomena*, 372:31–51, 2018.
- A. P. E. Bartos, B. Kaszás, and G. Haller. haller-group/tbarrier: Tbarrier (v1.0.0), 2023. URL <https://doi.org/10.5281/zenodo.6779400>.
- S. P. H. Boroujeni, A. Razi, S. Khoshdel, F. Afghah, J. Coen, L. O'Neill, P. Fule, A. Watts, N. Kokolakis, and K. Vamvoudakis. A comprehensive survey of research towards ai-enabled unmanned aerial systems in pre-, active-, and post-wildfire management. *Information Fusion*, 108:102369, 2024. ISSN 1566-2535.
- A. E. BozorgMagham, S. D. Ross, and D. G. Schmale III. Real-time prediction of atmospheric Lagrangian coherent structures based on forecast data: An application and error analysis. *Physica D: Nonlinear Phenomena*, 258:47–60, 2013.
- G. M. Byram. Combustion of forest fuels. in ‘forest fire: control and use’.(ed. kp davis) pp. 61–89, 1959.
- R. Bürger, E. Gavilán, D. Inzunza, P. Mulet, and L. M. Villada. Implicit-explicit methods for a convection-diffusion-reaction model of the propagation of forest fires. *Mathematics*, 8(6), 2020.
- N. P. Cheney, J. S. Gould, W. L. McCaw, and W. R. Anderson. Predicting fire behavior in dry eucalypt forest in southern australia. *Forest Ecology and Management*, 280:120–131, 2012.
- J. Coen. Modeling wildland fires: A description of the coupled atmosphere-wildland fire environment model (CAWFE). *NCAR Technical Note NCAR/TN-500+STR*, pages 1–38, 2015. doi: 10.1002/2013GL057868.
- J. Coen. Some requirements for simulating wildland fire behavior using insight from coupled weather–wildland fire models. *Fire*, 1(1):6, 2018.
- J. L. Coen, M. Cameron, J. Michalakes, E. G. Patton, P. J. Riggan, and K. M. Yedinak. WRF-Fire: coupled weather–wildland fire modeling with the weather research and forecasting model. *Journal of Applied Meteorology and Climatology*, 52(1):16–38, 2013.

- J. Curbelo and I. I. Rypina. A three dimensional lagrangian analysis of the smoke plume from the 2019/2020 australian wildfire event. *Journal of Geophysical Research: Atmospheres*, 128(21), 2023.
- S. Ducruix, D. Durox, and S. Candel. Theoretical and experimental determinations of the transfer function of a laminar premixed flame. *Proceedings of the combustion institute*, 28(1):765–773, 2000.
- F. Fendell and M. Wolff. Chapter 6 - wind-aided fire spread. In E. A. Johnson and K. Miyanishi, editors, *Forest Fires*, pages 171–223. Academic Press, San Diego, 2001. ISBN 978-0-12-386660-8. doi: <https://doi.org/10.1016/B978-012386660-8/50008-8>. URL <https://www.sciencedirect.com/science/article/pii/B9780123866608500088>.
- J. B. Filippi, F. Bosseur, C. Mari, and C. Lac. Simulation of a large wildfire in a coupled fire-atmosphere model. *Atmosphere*, 9(6):218, 2018.
- M. A. Finney, J. D. Cohen, J. M. Forthofer, S. S. McAllister, M. J. Gollner, D. J. Gorham, K. Saito, N. K. Akafuah, B. A. Adam, and J. D. English. Role of buoyant flame dynamics in wildfire spread. *Proceedings of the National Academy of Sciences*, 112(32):9833–9838, Aug. 2015. ISSN 0027-8424, 1091-6490.
- T. Hädrich, D. T. Banuti, W. Pałubicki, S. Pirk, and D. L. Michels. Fire in paradise: Mesoscale simulation of wildfires. *ACM Transactions on Graphics (TOG)*, 40(4):1–15, 2021.
- G. Haller. Lagrangian coherent structures. *Annual Review of Fluid Mechanics*, 47:137–162, 2015.
- G. Haller and G. Yuan. Lagrangian coherent structures and mixing in two-dimensional turbulence. *Physica D: Nonlinear Phenomena*, 147(3-4):352–370, 2000.
- T. R. Hudson, R. B. Bray, D. L. Blunck, W. Page, and B. Butler. Effects of fuel morphology on ember generation characteristics at the tree scale. *International Journal of Wildland Fire*, 29(11):1042–1051, 2020.
- A. Jarvis, A. H. Mardi, H. Foroutan, and S. D. Ross. Atmospheric transport structures shaping the “godzilla” dust plume. *Atmospheric Environment*, page 120638, 2024.
- E. Koo, P. J. Pagni, D. R. Weise, and J. P. Woycheese. Firebrands and spotting ignition in large-scale fires. *International Journal of Wildland Fire*, 19(7):818, 2010. ISSN 1049-8001.
- S. K. Lele. Compact finite difference schemes with spectral-like resolution. *Journal of Computational Physics*, 103(1):16–42, 1992.
- H. Li, N. Liu, X. Xie, L. Zhang, X. Yuan, Q. He, and D. X. Viegas. Effect of fuel bed width on upslope fire spread: an experimental study. *Fire technology*, 57:1063–1076, 2021.
- J. Mahoney, D. Bargteil, M. Kingsbury, K. Mitchell, and T. Solomon. Invariant barriers to reactive front propagation in fluid flows. *Europhysics Letters*, 98(4):44005, 2012.
- J. Mandel, J. D. Beezley, and A. K. Kochanski. Coupled atmosphere-wildland fire modeling with wrf 3.3 and sfire 2011. *Geoscientific Model Development*, 4(3):591–610, July 2011. ISSN 1991-9603.

- D. Morvan and N. Frangieh. Wildland fires behaviour: wind effect versus byram's convective number and consequences upon the regime of propagation. *International Journal of Wildland Fire*, 27(9):636–641, 2018.
- V. Motta, A. Guardone, and G. Quaranta. Influence of airfoil thickness on unsteady aerodynamic loads on pitching airfoils. *Journal of Fluid Mechanics*, 774:460–487, 2015.
- D. Or, E. Furtak-Cole, M. Berli, R. Shillito, H. Ebrahimian, H. Vahdat-Aboueshagh, and S. A. McKenna. Review of wildfire modeling considering effects on land surfaces. *Earth-Science Reviews*, 245:104569, 2023.
- L. Pareschi and G. Russo. Implicit–explicit runge–kutta schemes and applications to hyperbolic systems with relaxation. *Journal of Scientific Computing*, 25:129–155, 2005.
- J. G. Powers, J. B. Klemp, W. C. Skamarock, C. A. Davis, J. Dudhia, D. O. Gill, J. L. Coen, D. J. Gochis, R. Ahmadov, S. E. Peckham, et al. The weather research and forecasting model: Overview, system efforts, and future directions. *Bulletin of the American Meteorological Society*, 98(8):1717 – 1737, 2017.
- C. Reisch, A. Navas-Montilla, and I. Özgen-Xian. Analytical and numerical insights into wildfire dynamics: Exploring the advection–diffusion–reaction model. *Computers & Mathematics with Applications*, 158:179–198, 2024.
- C. G. Rossa and P. M. Fernandes. An empirical model for the effect of wind on fire spread rate. *Fire*, 1(2):31, 2018.
- T. K. Sengupta, G. Ganeriwala, and S. De. Analysis of central and upwind compact schemes. *Journal of Computational Physics*, 192(2):677–694, 2003.
- S. C. Shadden. Lagrangian coherent structures. *Transport and mixing in laminar flows: from microfluidics to oceanic currents*, pages 59–89, 2011.
- S. C. Shadden, F. Lekien, and J. E. Marsden. Definition and properties of lagrangian coherent structures from finite-time lyapunov exponents in two-dimensional aperiodic flows. *Physica D: Nonlinear Phenomena*, 212(3-4):271–304, 2005.
- C. C. Simpson, J. J. Sharples, J. P. Evans, and M. F. McCabe. Large eddy simulation of atypical wildland fire spread on leeward slopes. *International Journal of Wildland Fire*, 22(5):599–614, 2013.
- A. L. Sullivan. Wildland surface fire spread modelling, 1990–2007. 1: Physical and quasi-physical models. *International Journal of Wildland Fire*, 18(4):349–368, 2009a.
- A. L. Sullivan. Wildland surface fire spread modelling, 1990–2007. 2: Empirical and quasi-empirical models. *International Journal of Wildland Fire*, 18(4):369–386, 2009b.
- A. L. Sullivan. Wildland surface fire spread modelling, 1990–2007. 3: Simulation and mathematical analogue models. *International Journal of Wildland Fire*, 18(4):387–403, 2009c.
- R. Sun, S. K. Krueger, M. A. Jenkins, M. A. Zulauf, and J. J. Charney. The importance of fire–atmosphere coupling and boundary-layer turbulence to wildfire spread. *International Journal of Wildland Fire*, 18(1):50–60, 2009.

- C. S. Tarifa, P. P. D. Notario, and F. G. Moreno. On the flight paths and lifetimes of burning particles of wood. *Symposium (International) on Combustion*, 10(1):1021–1037, Jan. 1965. ISSN 00820784.
- A. Tohidi and N. B. Kaye. Stochastic modeling of firebrand shower scenarios. *Fire Safety Journal*, 91:91–102, 2017.
- S. Viknesh and K. Poddar. Active control of separated flow on a symmetric airfoil by pitching oscillation. *Physics of Fluids*, 33(8):087115, 08 2021. ISSN 1070-6631. doi: 10.1063/5.0060782. URL <https://doi.org/10.1063/5.0060782>.
- Z. D. Wilson, M. Tutkun, and R. B. Cal. Identification of Lagrangian coherent structures in a turbulent boundary layer. *Journal of Fluid Mechanics*, 728:396–416, 2013.